DE GRUYTER
OPEN

Acta Geophysica
vol. 64, no. 6, Dec. 2016, pp. 2550-2590
DOI: 10.1515/acgeo-2016-0069

Modelling and Observation of Mineral Dust Optical Properties over Central Europe

Michał T. CHILINSKI[1,2,5], Krzysztof M. MARKOWICZ[1],
Olga ZAWADZKA[1,2], Iwona S. STACHLEWSKA[1], Wojciech KUMALA[1],
Tomasz PETELSKI[3], Przemysław MAKUCH[3], Douglas L. WESTPHAL[4],
and Bogdan ZAGAJEWSKI[5]

[1]Institute of Geophysics, Faculty of Physics, University of Warsaw,
Warsaw, Poland; e-mail: mich@igf.fuw.edu.pl

[2]College of Inter-Faculty Individual Studies in Mathematics and Natural Sciences,
Warsaw, Poland

[3]Institute of Oceanology, Polish Academy of Sciences, Sopot, Poland

[4]Marine Meteorology Division, Naval Research Laboratory, Monterey, CA, USA

[5]Department of Geoinformatics and Remote Sensing, Faculty of Geography
and Regional Studies, University of Warsaw, Warsaw, Poland

Abstract

This paper is focused on Saharan dust transport to Central Europe/Poland; we compare properties of atmospheric Saharan dust using data from NAAPS, MACC, AERONET as well as observations obtained during HyMountEcos campaign in June 2012. Ten years of dust climatology shows that long-range transport of Saharan dust to Central Europe is mostly during spring and summer. HYSPLIT back-trajectories indicate airmass transport mainly in November, but it does not agree with modeled maxima of dust optical depth. NAAPS model shows maximum of dust optical depth (~0.04-0.05, 550 nm) in April-May, but the MACC modeled peak is broader (~0.04). During occurrence of mineral dust over Central-Europe for 14% (NAAPS) / 12% (MACC) of days dust optical depths are above 0.05 and during 4% (NAAPS) / 2.5% (MACC) of days

---

dust optical depths exceed 0.1. The HyMountEcos campaign took place in June-July 2012 in the mountainous region of Karkonosze. The analysis includes remote sensing data from lidars, sunphotometers, and numerical simulations from NAAPS, MACC, DREAM8b models. Comparison of simulations with observations demonstrates the ability of models to reasonably reproduce aerosol vertical distributions and their temporal variability. However, significant differences between simulated and measured AODs were found. The best agreement was achieved for MACC model.

Key words: aerosol, mineral dust, MACC, NAAPS, DREAM, aerosol transport model, remote sensing.

1. INTRODUCTION

Tropospheric aerosol influence on the global climate system, via direct and indirect radiative forcing, is important for understanding climate changes and still has a lot of uncertainties in geophysical studies (IPCC 2014). Among different types of aerosols, mineral dust may have a high influence on climate radiative forcing due to the possibility of events with large aerosol load and large aerosol optical depth. Natural sources of mineral dust aerosols (mainly silicates) are responsible for approximately 30% (Jimenez *et al.* 2009) of the total aerosol optical depth (AOD) in the atmosphere. Global soil-derived mineral dust emissions were estimated to be from 60 to 3000 Tg/yr by Duce (1995) and 1840 Tg/yr by Schutgens *et al.* (2012), which makes it the aerosol with the highest emissions globally. Relevant modification of radiation flux by mineral dust comes from scattering and absorption in both short and long-wavelength spectrum (Chen *et al.* 2011). The influence on climate is complex in the case of mineral aerosols and it could lead to either warming or cooling (Chand *et al.* 2009). Over surfaces with a relatively high albedo, over 0.3 (*e.g.*, over desert, snow), the top of the atmosphere (TOA) radiative forcing of mineral dust is usually positive and it will warm the climate system. On the other hand, over dark surfaces of albedo, lower than 0.15 (*e.g.*, over oceans, coniferous forests), the TOA radiative forcing of mineral aerosols usually is negative and make the climate system cooler. In the range between light and dark surfaces, where the albedo is higher than 0.15 and lower than 0.30 (Balkanski *et al.* 2007), the influence on climate can be in both directions and it depends on additional factors (*e.g.*, particles shape and size distribution, or particles refractive index). Those variables could be very different on a regional scale, which makes an estimation of mineral dust participation in global radiative forcing significantly uncertain (Balkanski *et al.* 2007). From an observer’s point of view, selecting an appropriate technique for determining mineral dust radiative forcing is a complex issue due to three main factors: assumptions in particle shapes and related parameterizations of non-spherical particles used in many retrieval algorithms (Wang *et al.* 2013); insufficient number of measurements in the infrared spectral range where, in general, dust strongly interferes with radiation with the same strength as solar radiation (Vogelmann *et al.* 2003, Markowicz *et al.* 2003); and difficulties in a strict distinction of aerosol type during measurements (Sinha *et al.* 2012).

The most important sources of mineral dust particles over southern, western and Central Europe are the arid and semi-arid regions in Northern Africa, dominated by the presence of the world's largest hot desert, Sahara (Prospero *et al.* 2002). The amount of Saharan dust production plays an important role for the climate of the whole Earth (Guerrero-Rascado *et al.* 2009). The Saharan dust transport over Europe strongly depends on complex meteorological conditions (Di Sarra *et al.* 2001) which makes it irregular, with greater intrusion's frequency and dust load amount during spring and summer months (Papayannis *et al.* 2008, Pisani *et al.* 2011). Studies of the North African dust emission and transport reveal the highest production of dust during the May-August period (Engelstaedter *et al.* 2006), however the main transport trajectories are different between March-May and July-August (Isrealevich *et al.* 2003). Spring trajectories show transport of dust emitted during sand storms in the western direction, to the area of the Atlantic Ocean, where dust on higher altitudes can reach the central and northern areas of Europe. Summer transport of the dust is mainly in the northern direction which results in high occurrence of dust events in southern Europe and in many cases it eventually directs the transport through the Alps to reach Central Europe (Varga *et al.* 2013). Most of these dust events occur in the Mediterranean area and only a few of them reach the borders of Poland (Papayannis *et al.* 2005, 2008; Mona *et al.* 2012). Dust climatological studies based on simulations of the NAAPS model in the period of 9 years (1998-2006) showed that dust events in Poland occurred mainly in the spring (with the highest annual peak in May) and autumn, during October and November (Maciszewska *et al.* 2010). Regarding the irregularity of dust events appearance, it is uncertain what is the real impact of Saharan dust on aerosol radiative forcing over Central Europe, which motivates further research of dust impact on radiative forcing over Poland.

The best source of information on the dust physical and chemical properties comes from field campaigns (Formenti *et al.* 2008, Osborne *et al.* 2008, Heintzenberg 2009, Kandler *et al.* 2009, Tesche *et al.* 2009, Gross *et al.* 2011, Marsham *et al.* 2013) and by the model simulation. Lidar techniques are useful in atmospheric aerosol studies as they can provide data about aerosol properties with high temporal and spatial resolutions. Retrieval of information on the aerosol properties from lidar measurements is complex and requires the use of multi-wavelength lidars and/or additional data from different devices along with several assumptions (Weitkamp 2005). The other important remote sensing method involves passive observations with sun-photometers, which integrate optical properties of a whole air column providing accurate AOD and Angstrom exponent measurements. Measurements from sun-photometers can be used as an input for lidar retrieval algorithms (Landulfo *et al.* 2003, Lopes *et al.* 2013). Apart from remote sensing methods, *in situ* measurements of absorption coefficient with aethalometers and scattering coefficient with nephelometers are of great importance. Data obtained by the two latter instruments contribute to improve the information on the lowermost air layer, which usually is invisible for lidars due to the incomplete overlap between the emitted laser beam and the receiver's field of view (Guerrero-Rascado *et al.* 2010, Wandinger and Ansmann 2002). Thus, the athelometer-nephelometer (with polar nephelometer capable of measuring backward scattering) combined observations can deliver data for assumptions of a lidar ratio necessary for a simple elastic lidar or ceilometer data retrieval (Markowicz *et al.* 2008). Due to difficulties in conducting systematic field measurements and a sparse grid of measurement stations, it is very important to collect field data during dust events, which could be used for verifying of model simulations accuracy. Although the presented dust optical depths (DOD) values over Poland are small in comparison to the basin of Mediterranean Sea, it is still around 25% of total AOD in our region and mineral dust is one of the two most important types of aerosols above the boundary layer (together with products of burning). This fact, together with the lack of models' validations in Central Europe/Poland (area far from sources of dust), especially DREAM and NAAPS, was the main motivation for our study.

The aim of research described in this paper is an attempt to utilize different modelling and observation techniques to estimate the seasonal variation of the dust optical properties over Poland. This paper presents the findings of a field campaign in Karpacz, South-Western Poland, during the Hyperspectral Remote Sensing for Mountain Ecosystems (HyMountEcos) project conducted in June-July 2012. Location of the field campaign site is presented on the overview map (Fig. 1). During this campaign, measurements were performed with lidar, ceilometer, sun-photometers. The whole event was simulated by the DREAM8b, NAAPS and MACC models. These models are briefly described in the Section 2. Section 3 is dedicated to the instruments used during the campaign and different retrieval techniques used to evaluate the lidar and ceilometer data. Section 4 describes the long-term variability of the dust optical properties based on the NAAPS and MACC models and AERONET station in Belsk. In Section 5, the results of the field campaign are described (Holben *et al.* 1998), beginning with temporal evolution of lidar and model results and ending with a comparison of vertical profiles of aerosol extinction obtained from lidar, ceilometer and model simulations.

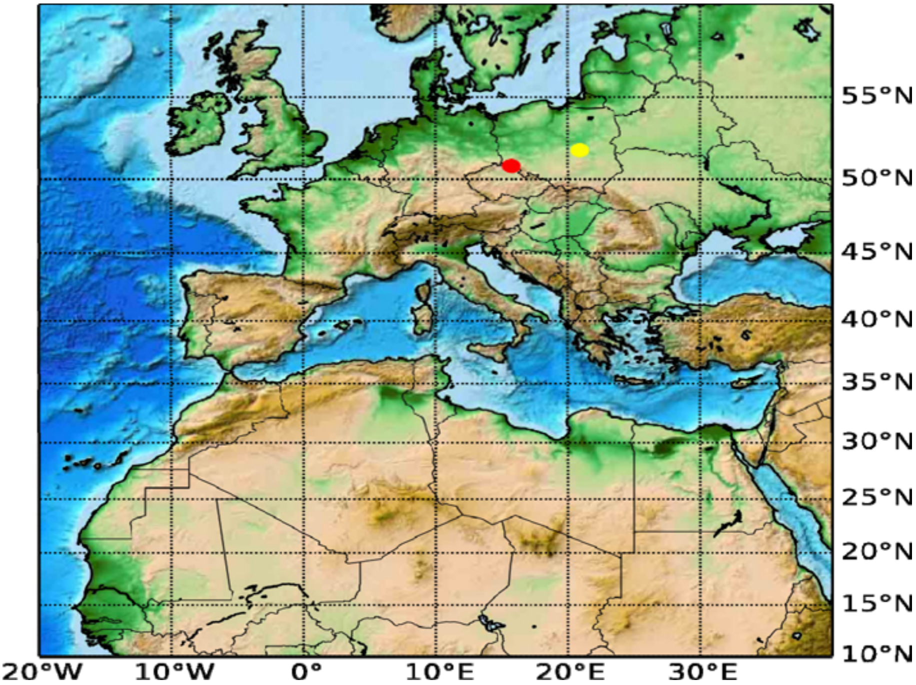

Fig. 1. Overview map with hypsometry and countries boundaries of Western and Central Europe and North Africa. HyMountEcos (Poland) – red circle, Belsk (Poland) AERONET station – yellow circle.

2. AEROSOL TRANSPORT MODELS

To simulate mineral dust optical properties, the Dust Regional Atmospheric Modeling (DREAM8b) (Perez *et al.* 2006a, b) was used. For better time resolution the model was especially run for the HyMountEcos event analysis only, while for the climatological study the data from the public repository of DREAM8b simulation hosted by Barcelona Supercomputing Center was used. To initialize the model for case study description, we used two months of meteorological data prior the period of HyMountEcos campaign. The original DREAM model (Nickovic *et al.* 2001) is a model developed to simulate and predict the atmospheric cycle of a mineral dust aerosol on a regional scale. The model is based on a partial differential nonlinear Eulerian-type equation for a dust mass continuity. Fundamental for all models of atmospheric mineral dust cycle is the parameterization and the conditioning of the dust production phase. In the DREAM the parameterization of aeolian erosion of soil is driven by the soil moisture, the type of soil, type of vegetation, and the atmospheric surface turbulence. As an input for the production components, a global data set on land cover is used with additional data from the Food and Agriculture Organization of the United Nations (FAO) 4 km soil texture data set is required to determine particle size parameters. Grid points from arid and semiarid categories of the global U.S. Geological Survey (USGS) 1 km vegetation data set are treated as potential sources of dust. Particle size distribution is divided into the 8 size bins with the following effective radii: 0.15, 0.25, 0.45, 0.78, 1.3, 2.2, 3.8, 7.1 micrometers. The initial atmospheric and boundary conditions are the 12 UTC 0.5 × 0.5 degree global National Centers for Environmental Prediction (NCEP) forecast data sets obtained via the Global Forecast System (GFS) model. The 24 h forecast from the day before defines the initial conditions of a dust cycle for the next forecast.

Dust optical depth (DOD) from DREAM8b model is computed from the following equation

$$\tau(\lambda) = \sum_{i=1}^{8} \tau_i(\lambda) = \sum_{i=1}^{8} \frac{3}{4 r_i \rho_i} M_i Q_{\mathrm{ext}}^{i}(\lambda) \tag{1}$$

where r_i is an effective radius, ρ_i is a particles mass density, M_i is a column mass loading, Q^{i}_{ext} is an effective extinction cross section for each particle bin. Within each aerosol size bin, dust particles are assumed to have a time-invariant sub-bin lognormal distribution with number median radius of the distribution 0.2986 and geometric standard deviation of 2.0 (Perez *et al.* 2006a, b). The effective extinction cross-section for each particle bin is calculated for spherical particles based on Lorentz–Mie theory. The dust refractive index at 550 nm is assumed to be 1.53 + 0.0055*i* (Hess *et al.* 1998); however, recent studies propose lower values of refractive index, between –0.0005 and –0.0014 (McConnell *et al.* 2008). The Angstrom exponent is computed from Eq. 1 applied for wavelengths of 550 and 1000 nm.

The NAAPS re-analysis model (Witek *et al.* 2007, Zhang *et al.* 2008) is used to predict the spatial distribution of the aerosol concentration and optical properties from 1998 to 2006 and between 2011 and 2012. NAAPS is based on a modification to the model developed by Christensen (1997) with its transition to the Fleet Numerical Meteorology and Oceanography Center (FNMOC). The NAAPS model output is available as 1 × 1 degree, at 6-hour intervals and 25 sigma-coordinate levels. Model solves the advection-diffusion equation at each grid point for each species. The advection and turbulent mixing is controlled by Navy Operational Global Atmospheric Prediction System (NOGAPS) (Hogan and Rosmond 1991, Hogan and Brody 1993), a dynamic model providing global meteorological fields. Satellite-derived aerosol observations from MODIS assimilated into NAAPS provide estimates of AOD above oceans (Zhang *et al.* 2008). The current version of NAAPS includes gaseous SO_2 and four aerosol components: mineral dust, sea salt, particulate sulphates (SO_4) and smoke. Mineral dust emission areas are characterized by the U.S. Geological Survey (USGS) Land Cover Characteristic Database (Anderson *et al.* 1976). Dust is lifted from the surface whenever the friction velocity exceeds a threshold value (0.6 m/s) and the surface moisture is less than 30%. The employed emission parameterization is proportional to friction wind (Westphal *et al.* 1988). The NAAPS model includes only one size bin for each aerosol type. Aerosol optical properties, such as AOD, single scattering albedo, asymmetry parameter and Angstrom exponent for each aerosol type and as well as for external mixture of particles are computed every 6 hours based on optical interface (Maciszewska *et al.* 2010). NAAPS utilizes a database of global sources individual for each of the simulated aerosol species. Source estimates incorporate weather, remote sensing and anthropogenic activity. For each type of emissions, emission factors are defined, which, for smoke, depend on land use, fuel loading, fuel type and frequency of burns in a particular area; for mineral dust the main factors are: type of soil, area of soil patch and humidity.

The MACC global aerosol transport model consists of ECMWF's Integrated Forecasting System (forward model) and a data-assimilation module (Bellouin *et al.* 2013). The forward modules include 12 prognostic variables (11 aerosol mass mixing ratios and one precursor, SO2). All aerosol species are treated as tracers in the forward model vertical diffusion and convection schemes and are advected by the semi-Lagrangian scheme, consistently with all other dynamical fields and tracers (Morcrette *et al.* 2009). Five types of tropospheric aerosols are included: sea salt, desert dust, organic matter, black carbon and sulphate aerosols. Mineral dust and sea salt are represented by 3 different size classes. Desert dust bins are defined with radii between 0.03-0.55, 0.55-0.9, and 0.9-20 μm, which correspond about 10, 20, and 70% of the total dust mass for each aerosol bins. Emissions of dust particles depend on modelled near-surface wind speeds and dust emission potential which is a function of soil morphology (Ginoux *et al.* 2001). AOD of each aerosol species are computed based on the assumption of external mixture and from standard Lorentz-Mie algorithm (Morcrette *et al.* 2009). Data assimilation module includes the ECMWF four-dimension variation which accounts for background and observational errors. The assimilated observation is the MODIS AOD at 550 nm retrieved over ocean and dark land surface. Aerosols of each type are corrected in proportion of their original contribution to the total aerosol mass (Benedetti *et al.* 2009). In this study we used the MACC re-analysis available for the period between 2003 and 2012.

3. INSTRUMENTATION AND DATA EVALUATION DURING FIELD CAMPAIGN

The measurements for the case study were collected during the first part of the HyMountEcos campaign. This international Polish–Czech project was focused on the assessment of the benefit of hyperspectral techniques for monitoring the highly valuable mountain ecosystems of the Giant Mountains (Karkonosze) National Park. The first part of the field campaign started on 26 June 2012 and finished on 10 July 2012. During the experiment, the mobile laboratory of the Institute of Oceanology, Polish Academy of Sciences (IOPAS) and the Institute of Geophysics, Faculty of Physics, University of Warsaw (IGFUW), equipped with remote sensing, *in situ* and meteorological devices were deployed on the outskirts (about 1 km) of a small town of Karpacz in the Karkonosze in south-western part of Poland. The measurements were made at a field station located 690 m a.s.l. (50.765 °N, 15.757 °E), on the northern side of Sniezka, the highest peak of the Karkonosze Mountains (1602 m a.s.l.). The station was situated over 100 m above the bottom of the valley where Karpacz town is located. The measurement area was situated in a forest clearing, approximately 40 m from the wood areas. The surrounding spruce forest protected the clearing from strong winds. The nearest human settlements, which could cause air pollution, were located about 250 m from the field station; however, both were separated by the ravine of a mountain stream, whose ridges were thickly wooded.

The mobile laboratory was equipped with a LB-10 elastic backscattering lidar operating at 532 nm (Raymetrics, Greece), a CHM-15k ceilometer operated at 1064 nm (JenOptik, Germany), a whole-sky camera, two Microtops II sun-photometers (Solarlight, USA), and a weather station WXT510 (Vaisala, Finland).

3.1 Sun-photometers

In this study, the measurements from the two Microtops II sun-photometers were used. The handheld spectral Microtops II sun-photometers (Morys *et al.* 2001) with visible and near-infrared wavelengths allowed to retrieve aerosol optical depth AOD at 380, 500, 675, 870, and 1020 nm. An important issue in data quality assurance involved the proper calibration of the sun-photometers (Smirnov *et al.* 2000). The calibration factors were derived during different dedicated calibration campaigns in 2012 on Tenerife, Spain, and in Sopot, Poland, as well as in 2011 at Zugspitze, Germany. The spectral dependence of the AOD – the Angstrom exponent is sensitive to the calibration coefficients (Shifrin 1995). In this study, we use the Angstrom exponent defined by AOD at two wavelengths (500 and 1020 nm). Uncertainty of Angstrom parameter decreases significantly with the rise of the AOD value and for the AOD of 0.05, 0.1, and 0.2 (at 500 nm) is about 32, 15, and 8%, respectively (Wagner and Silva 2008, Zawadzka *et al.* 2013).

In addition, data from a CIMEL CE 318 sun photometer (www.cimel.fr) mounted at AERONET station in Belsk (51.836°N, 20.789°E, 180 m a.s.l.) are used. The sun photometers CIMEL are a multi-channel, automatic sun-and-sky scanning radiometers that measure direct solar irradiance and sky radiance at the Earth's surface at seven wavelengths (380, 440, 500, 675, 870, 936, and 1020 nm). The AOD is retrieved at 6 channels and 936 nm channel is used to estimate the total water vapor column. In this study we used the lev. 2.0 data collected between 2002 and 2012.

3.2 Ceilometer and lidar

In principle, JenOptik's CHM15k, similarly to other ceilometers (*e.g.*, Vaisala CT25K), is designed to detect cloud base height (Martucci *et al.* 2010) with the use of lidar technology (O'Connor *et al.* 2004), providing reliable information on clouds up to 15 km. However, significantly higher signal-to-noise ratio than for other ceilometers allows to apply CHM15K to determine the mixing height (Eresmaa *et al.* 2006, Münkel *et al.* 2004, Stachlewska *et al.* 2012) and to examine aerosol profiles up to middle troposphere (Sundström *et al.* 2009, Markowicz *et al.* 2012, McKendry *et al.* 2009, Flentje *et al.* 2010, Frey *et al.* 2010, Heese *et al.* 2010).

The CHM15k uses a diode-pumped Nd-YAG laser at 1064 nm, yielding about 8 μJ per pulse at 5-7 KHz repetition rate (Wiegner and Geiß 2012). The CHM15k receiver consists of 12.7 cm lens telescope directing the backscattered laser light to a silicon avalanche photodiodes (APD) with a photon counter. The divergence of the laser beam is 0.1 mrad. The vertical resolution of the instrument is 15 m. During the field campaign discussed in this paper the temporal averaging was set to 30 s.

The Raymetrics elastic lidar LB-10 is designed to perform continuous measurements of aerosol particles. It is based on the second harmonic frequency of a compact Nd:YAG laser, which emits pulses of 20 mJ output energy at 532 nm with a 20 Hz repetition rate. The laser beam diameter is 10 mm with divergence of less than 0.1 mrad. The optical receiver is a Cassegrainian reflecting telescope with a primary mirror of 20 cm diameter, directly coupled to the lidar signal detection box. Analog detection of the photomultiplier current and single photon counting are combined in one acquisition system. The combination of a powerful A/D converter (12 Bit at 40 MHz) with a 250 MHz fast photon counting system increases substantially the dynamic range of the acquired signal, compared to conventional systems and provides a spatial resolution of 7.5 m. The lidar overlap height was estimated to be between 300 and 400 m based on the visual inspection of the vertical variability or the range corrected signal.

Thanks to data from two laser systems operating on two different wavelengths (532 and 1064 nm) it is possible to detect cases where extinction coefficient is higher at infrared than at visible range, which could indicate coarse particles in the atmosphere, which are characteristic for mineral dust occurrence.

3.3 Other data

The data analyzes were supported with observations from a Cloud-Aerosol Lidar with Orthogonal Polarization (CALIOP) mounted onboard a Cloud-Aerosol Lidar and Infrared Pathfinder Satellite Observations (CALIPSO) satellite (Wong *et al.* 2013). In addition, a Hybrid Single Particle Lagrangian Integrated Trajectory Model (HYSPLIT) (Draxler and Rolph 2010) is used to describe the origin of the air masses.

3.4 Dust properties retrieval techniques

To obtain the vertical profiles of the extinction and backscatter coefficient from lidar and ceilometer signals, the standard Klett–Fernald–Sasano approach was used (Klett 1985, Fernald 1984, Sasano *et al.* 1985). This method requires knowledge or an assumption of the aerosol backscatter coefficient at reference altitude and additional information on aerosol optical properties, such as AOD and/or lidar ratio. In case of lidar and ceilometer data, the standard backward and forward methods (Markowicz *et al.* 2008) were applied, respectively. In the first case we assumed that at the reference altitude is 8 km a.g.l. In the case of forward approaches, the initial aerosol extinction coefficient (at 0.25 km) was assumed to be 0.05 km^{-1} at 1064 nm and initial lidar ratio is set of 35 srad at 1064 nm. The last value is typical for mineral dust particles (Wang *et al.* 2008, Pappalardo *et al.* 2013). However, during the consecutive iterations the initial value varied, so that the final aerosol extinction coefficient at 0.25 km usually differs from the starting value. The same concerns the lidar ratio which is adjusted due to the lidar ratio typical for dust events and additionally verified by AOD constraint calculated from Angstrom exponent for coarse mode, with extinction for 1064 taken from ceilometer retrieval. The assumed AOD was validated by the NAAPS and MACC results and fits inside the simulated range of AOD. In both the backward and forward approach, it was assumed that in the upper troposphere it is only the molecular scattering that contributes to the total backscatter coefficient. Assuming an error of 2% of the molecular backscatter coefficient calculated from the radio sounding data, which is accounted for a daily variation of temperature and pressure, the error of the retrieved aerosol extinction coefficient is about 10% (Stachlewska and Ritter 2010). The errors resulting from the assumption of the overlap correction function (remaining unchanged with time between 250 and 600 m) are less than 3% (Stachlewska *et al.* 2010).

4. ANNUAL VARIABILITY OF THE DUST OPTICAL PROPERTIES

In this section we present results of long-term (1998-2006, 2011, 2012) NAAPS, MACC (2003-2012) re-analysis and DREAM8b v 2.0 re-analysis (2006-2012) as well as the 11-year (2002-2012) observation of the AOD at the AERONET station in Belsk (51.836°N, 20.789°E, 180 m a.s.l.). NAAPS is a global aerosol analysis and prediction model, which operates on $1^o \times 1^o$ grid with meteorology from NOGAPS with the same resolution. DREAM8b as a regional model has a domain in the range of 5S to 70N and 60W to 90E with $0.3^o \times 0.3^o$ horizontal resolution; meteorology is driven by GFS $0.5^o \times 0.5^o$ products. Both models use 6-hour update cycle and data is reported with this time step. MACC is the acronym for the atmospheric composition monitoring project and data published by the project repositories comes from the ensemble of models with different parameters and resolutions (Marécal *et al.* 2015). Resolution and input data for described models show that they are suitable for mesoscale simulations and with too sparse resolution for analyzing of microscale events. Figure 2 shows (top) dust AOD at 550 nm, (middle) dust to total AOD ratio at 550 nm, and (bottom) relative number of days with dust AOD higher than 0.05 for both NAAPS (gray bars), MACC (black bars), and DREAM (white bars). The 0.05 threshold for dust events was selected arbitrarily, to select days with dust contribution to the AOD of about 25%. In case of both models, the dust AOD shows annual cycle with minimum (0.01-0.02) during winter and maximum (about 0.05) during spring and summer. Differences between MACC and NAAPS models are small with the exception of the summer months. During this period the dust AODs in case of MACC are larger (about 0.01) than NAAPS data. In case of DREAM model the dust AOD is significantly smaller, with maximum during May and June. The long-term dust AOD at 550 nm is for NAAPS 0.031, MACC 0.028, and DREAM only 0.005, which correspond to mean dust contribution to the total AOD of 17 and 15% in case of NAAPS and MACC, respectively. In case of NAAPS data the ratio of dust to total AOD has a maximum peak in May (0.28) and a minimum in December (0.1). However, the MACC annual amplitude is smaller and this ratio varies between 0.1 and 0.2. Similarly to dust AOD case during summer months, the MACC shows larger dust contribution to the total AOD than the NAAPS model. In addition, there is a positive difference between NAAPS and MACC ratio of dust to total AOD during spring period. Similar temporal

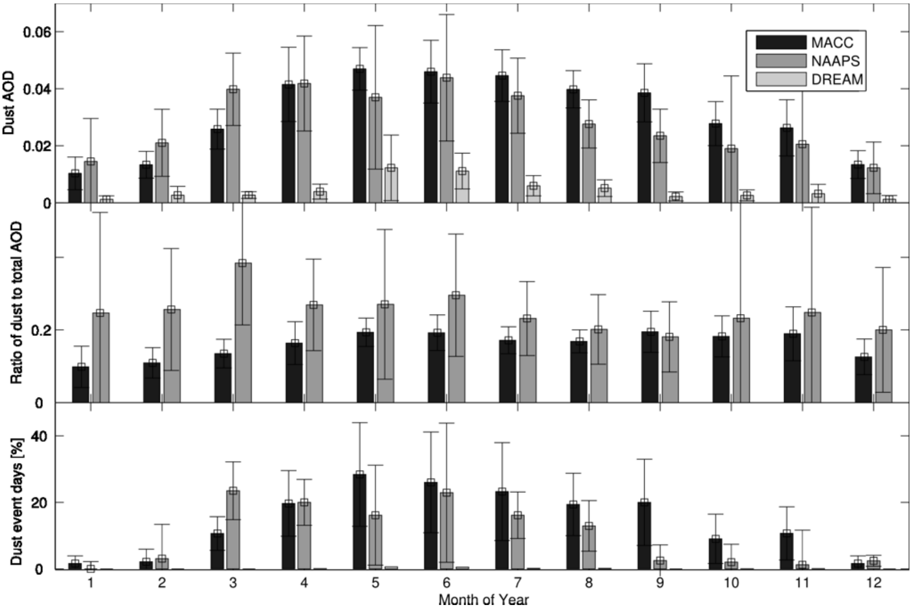

Fig. 2. The long-term monthly mean of dust AOD at 550 nm (top), dust to total AOD (middle), and relative number of days in % with dust AOD larger than 0.05 (bottom) obtained from MACC (black bars), NAAPS (gray bars), and DREAM (white bars) for Poland. Whiskers on bars represent standard deviation.

variation shows the frequency of the dust events. Bottom panel of the Figure 2 shows percentage of days with dust AOD higher than 0.05 (the threshold value was chosen arbitrarily). During May, both models show about 28% of days with dust transport while during winter these values are below 5%. The annual means of these parameters are 12 and 14%, respectively, for MACC and NAAPS model. For threshold of 0.1 the NAAPS models show dust event in May during 9.5% days and only during 4.5% days in case of MACC. In this case, during the whole year, the NAAPS shows about 4% and MACC 2.5% days with a dust event. In simulations from DREAM model the dust events are almost absent, even during the spring maximum.

The largest differences between models appear during summer months and to figure out this discrepancy we did some additional studies. Figure 3 shows the monthly mean dust AOD averaged over Northern Africa (between 30° and 33°N and 10°W and 45°E) based on NAAPS (gray bars) and MACC (black bars). The line with squares corresponds to relative number of days with transport of air masses from Africa to Central Poland. These days are selected using the HYSPLIT back-trajectories ending in Central Poland at 1.5 and 4 km that passed the Northern Africa. Similarly to dust AOD over

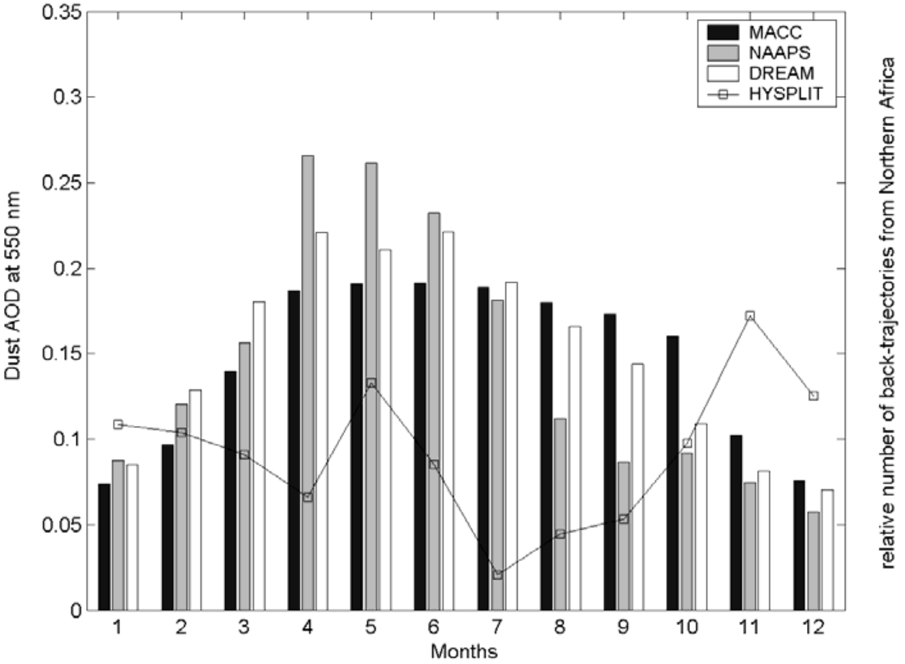

Fig. 3. The monthly mean dust AOD at 550 nm averaged between 30° and 33°N and –10°W and 45°E (North Africa) for MACC (black bars), NAAPS (gray bars), and DREAM (white bars) as well as the relative number of days with back-trajectories crossing North Africa and ending over Central Poland at 12 UTC.

Poland, values for Northern Africa show larger amplitudes in case of NAAPS model. The spring peak exceeds 0.25 at 550 nm while MACC maximum period appears between spring and summer and does not exceed 0.2. For Sahara region the DREAM model shows similar annual cycle as the NAAPS with a significant transition between spring and autumn. NAAPS and DREAM annual cycles are consistent with previous studies which show the maximum of dust emission over Sahel during spring months (Brooks and Legrand 2000, Goudie and Middleton 2001) and late-spring to monsoon onset (Engelstaedter and Washington 2007, Marsham *et al.* 2008). Dust emission is related to the passage of cyclonic fronts in the Northern Sahara in the late winter and spring months and moist convective systems in the Sahel and Southern Sahara in summertime (Alpert and Ziv 1989, Tegen *et al.* 2013). However, more recent results obtained from Multiangle Imaging Spectroradiometer (MISR) by Choobari *et al.* (2014) indicate that AOD over Northern Africa is similar during spring and summer months, which is more consistent with MACC results. However, the back-trajectories show the possible most intensive transport of Saharan air masses to Central Europe in May and November. Both models indicate peak of the dust AOD over Poland in May. During November the intensive transport of Saharan air mass is high but the dust emission is quite low and therefore the dust AOD in Poland is not as large as during May. The minimum of Saharan air mass transport frequency is during summer months (July, August, September) which agrees with reduction of dust AOD simulated by NAAPS. This temporal variation is not predicted by the MACC model which can be explained by data assimilation problems. In case of MACC, the AOD from MODIS is assimilated into the model but each aerosol type is corrected in proportion of its original contribution to the total aerosol mass (Benedetti *et al.* 2009). Therefore, relatively high MACC dust AOD during summer months can be explained by an increase of total AOD during this period. Long-term observation of AOD in Belsk AERONET station shows maximum in July and August. It is important to mention that we used 96-hour back-trajectories simulated by HYSPLIT, which results in a possible loss of data from longer and more complicated dust transport cases. Additionally, due to meteorological situation and processes of deposition, it is possible that not every trajectory from above Africa transports dust to Poland (AERONET (2002-2012)).

More information about model discrepancy can be found from model validation with AERONET observations. Figure 4a and b shows comparison of the total AOD at 550 nm simulated by both models and measured at AERONET in Belsk. In case of Belsk data, the AODs at 55 nm are computed from 500 nm AOD and from Angstrom exponent. In case of MACC model, the mean bias is only 0.02, RMSE is 0.1, and squared correlation co-

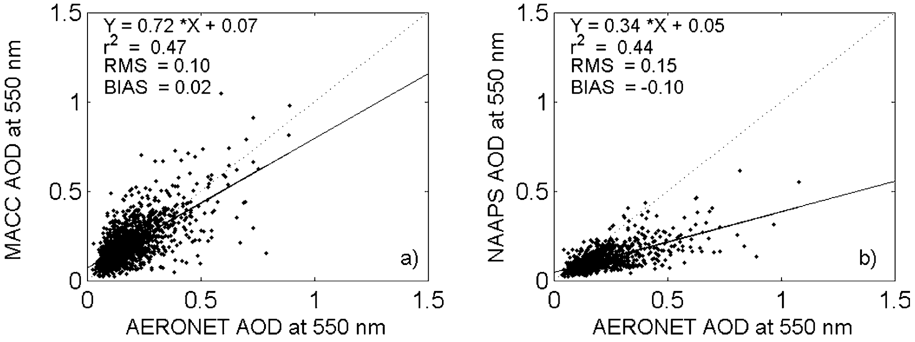

Fig. 4. Comparison of AOD at 550 nm measured in frame of AERONET (lev. 2.0) in Belsk with MACC (a) and NAAPS (b) model. Dotted line corresponds to perfect agreement and solid line is a liner fit.

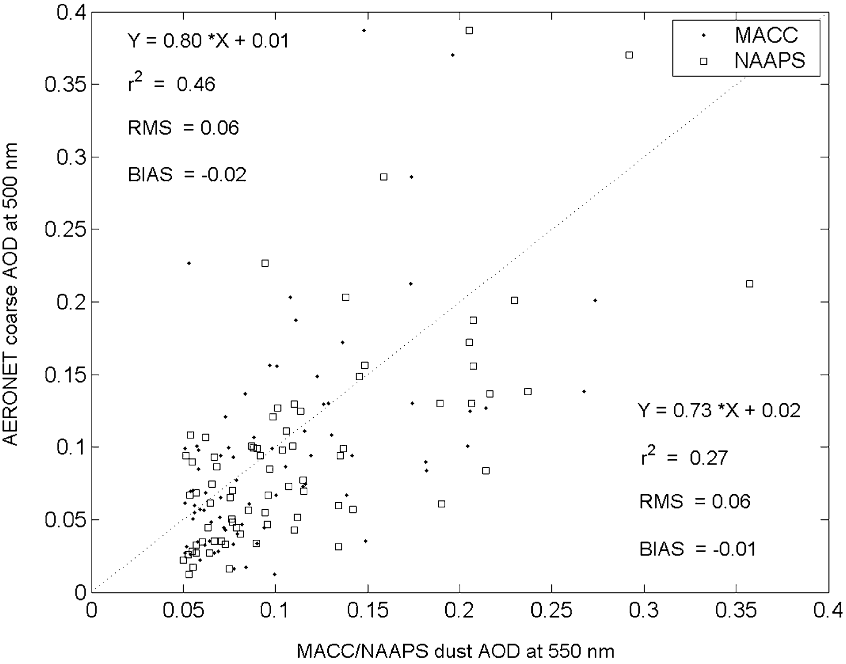

Fig. 5. Comparison of the dust AOD 550 nm obtained from MACC (dots) and NAAPS (squares) models with AERONET AOD of coarse mode at 500 nm retrieved from direct measurements (lev. 2.0). Upper left statistics are for MACC and lower right for NAAPS model.

efficient r^2 is 0.47. The NAAPS model significantly underestimates the AOD (mean bias –0.1); RMSE is 0.15 and r^2 is 0.44. The good agreement for MACC is possibly an effect of AOD assimilation over land. In case of NAAPS model, deficiencies influence simulation accuracy, especially insufficient representation of anthropogenic aerosols and simplified parameterization of aerosol optical properties (only one particle bin size) (Maciszewska *et al.* 2010) as well as the lack of assimilation of the AOD. In case of dust event, defined when the dust AOD for both model is higher than 0.05, we found a better correlation (r^2 is 0.58 and 0.50 for MACC and NAAPS) but a larger bias (0.04 and –0.15 for MACC and NAAPS). Although dust aerosol has better parameterization in the NAAPS than anthropogenic aerosol, we found worst agreements with AERONET data due to the fact that during long-range transport the dust particles are usually mixed with aerosol of other type (Bègue *et al.* 2012; Pavese *et al.* 2012; Papayannis *et al.* 2008). However, the comparison of the AOD obtained from NAAPS and from AERONET coarse mode looks more consistent (Fig. 5). The mean bias is only 0.01 and RMSE is 0.06. Similar results have been found for MACC

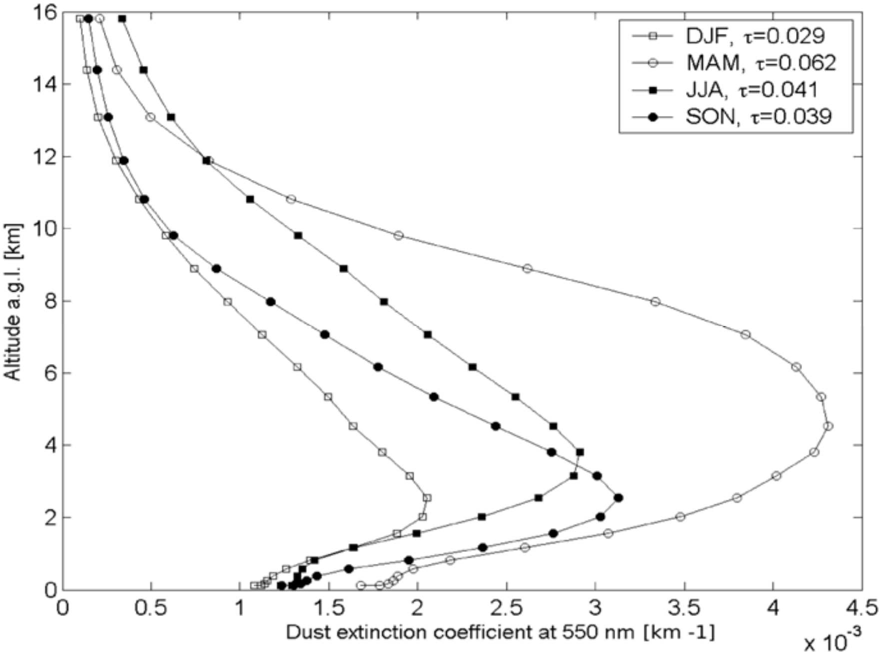

Fig. 6. The mean profiles of dust extinction coefficient obtained from NAAPS re-analysis for December-January-February (open-square line), March-April-May (open-circle line), June-July-August (solid-square line), and September-October-November (solid-circle line).

model. Note that AERONET coarse mode of AOD was estimated for 500 and model AOD at 550 nm. However, in case of coarse mode we cannot expect significant spectral dependence of the AOD. The comparison of the dust AOD by coarse mode AOD is only a simplification because other aerosol species can contribute to it (for example, sea salt or local dust particles, but we do not expect their significant impact on the area of study).

The vertical variability of dust optical properties was obtained only from NAAPS model because the web interface to MACC re-analysis includes only the AOD product. Figure 6 shows the long-term mean of the dust extinction profiles averaged for winter (open squares), spring (open circles), summer (solid squares), and autumn (solid circles). The averaged profile of extinction indicated that dust layers may appear in the upper troposphere. Previous lidar measurements have shown dust mostly in the middle troposphere (Begue *et al.* 2012) but also in the upper troposphere (Ansmann *et al.* 2003). The altitude of maximum dust extinction varies between 2.5 and 3 km in winter and autumn, to 4 km in summer and to 5 km in spring. The maximum of dust extinction coefficient changes between 2 and 4.3×10^{-3} km^{-1}.

Dust is more elevated in summer than in winter, which is in consistence with results of 5-year CALIPSO climatology (Huang *et al.* 2013). After analysis of the whole dataset from three different models we can conclude their performance with the following observations: the NAAPS, although without special assimilation, predicts local emissions well; MACC as an ensemble assimilate data from satellite products, thus predict AODs with high correspondence to observations; DREAM8b is the only model in this set dedicated only to mineral dust transport cycle, which results in the lack of possibility to compare dust AOD to total AOD; simulations of DREAM8b emissions in North Africa fit the results modeled by other models, but after long-range transport simulations to the area of Central Europe/Poland, dust AODs significantly drop, below predictions of other models.

5. RESULTS OF FIELD CAMPAIGN

5.1 Overview of dust event in June 2012

In this section the results of experimental measurements and numerical simulations of a dust event which occurred between 28 and 31 June 2012 are presented. During this period a weak high-pressure system developed over Central and Eastern Europe and an intensive low-pressure system over Great Britain, whereby extensive atmospheric fronts were present. Generally, the synoptic chart predicted south-west circulation and advection of air masses from western Sahara, via the western basin of the Mediterranean Sea to Central Europe.

The series of 5-day backward trajectories generated with the NOAA HYSPLIT model (Fig. 7) indicate that at 18:00 UTC on 28 June 2012 air masses from all the analyzed levels arrived over our site from the Atlantic Ocean through Great Britain. 6 hours later, at 00:00 UTC on 29 June, the situation changed and the calculated source of air masses at the level of 3 and 5 km was in the western Sahara, which suggests a possible Saharan dust transport to Europe. From Africa to the HyMountEcos observational site in Karpacz, the air masses were advected via the Atlantic Ocean and Germany. Twelve hours later, simulation indicated the possible source of mineral dust, mainly on 1 km level, where air masses came from 2.5 km height over the western Sahara. The results from 00:00 UTC on 30 June show the end of potential dust sourcing in Sahara, as all levels had their particle sources across the Atlantic Ocean, from the Iberian Peninsula's coast at 1 km level to the Labrador coast at 5 km level height.

Figure 8 presents simulation of DOD distribution over Central Europe calculated by the MACC, DREAM8b, and NAAPS models. First panel (Fig. 8a) illustrates 00:00 UTC on 29 June 2012. Simulated DOD over Karpacz was MACC 0.19, DREAM8b 0.03, NAAPS 0.11. All models pre-

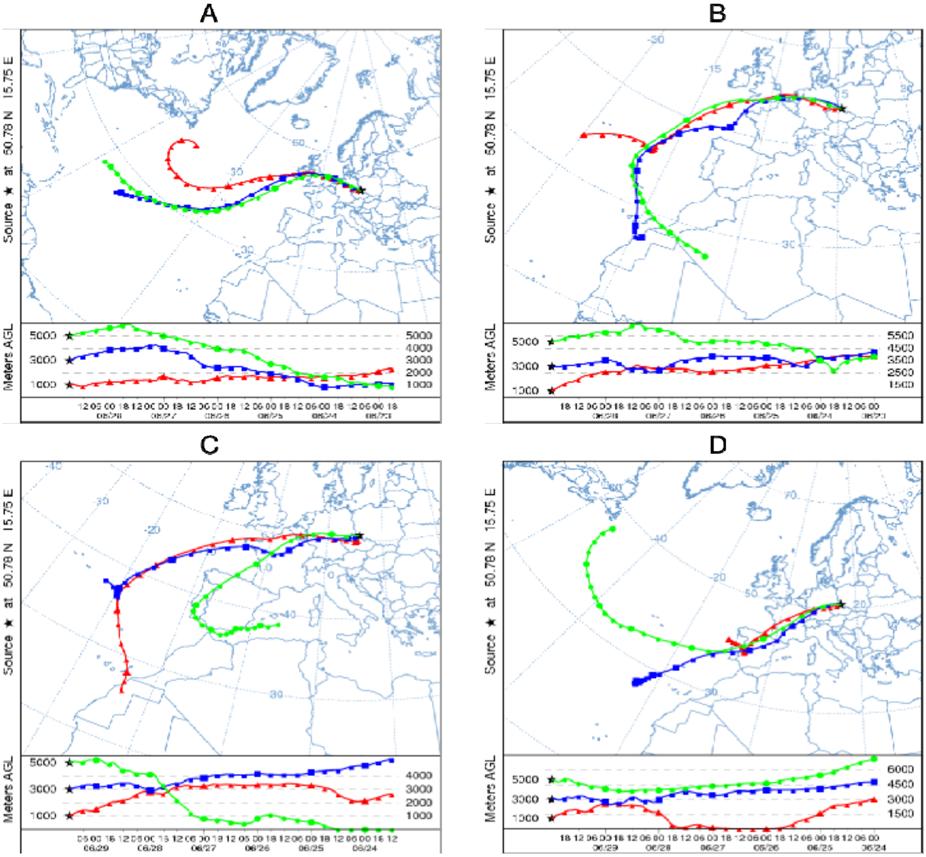

Fig. 7. Hybrid Single Particle Lagrangian Integrated Trajectory Model (HYSPLIT) backward trajectories obtained for Karpacz at: (A) 18 UTC on 28 June 2012, (B) 00 UTC, (C) 12 UTC on 29 June 2012, and (D) 00 UTC on 30 June 2012. HYSPLIT model was running for 5 days with meteorological data from the Global Data Assimilation System (GDAS).

dicted the highest DOD in the western part of Europe. Predicted spatial distribution shows an area of higher DOD coming from the north-west, but the exact location of dust is different among all models. The next panel (Fig. 8b) represents situation at 12:00 UTC on the same day. Models predicted further transport of dust to the east. As on the first panel, the DOD predicted by MACC has highest values (over 0.3 in Germany) and 0.21 over Karpacz. DREAM8b placed Karpacz on an edge of higher DOD with a value of 0.10. NAAPS presents different solution, where Karpacz (0.08) is in the middle between two areas of higher DOD. All models predicted sharp gradient of dust load between Great Britain (low values, 0.0-0.04) and Western Europe

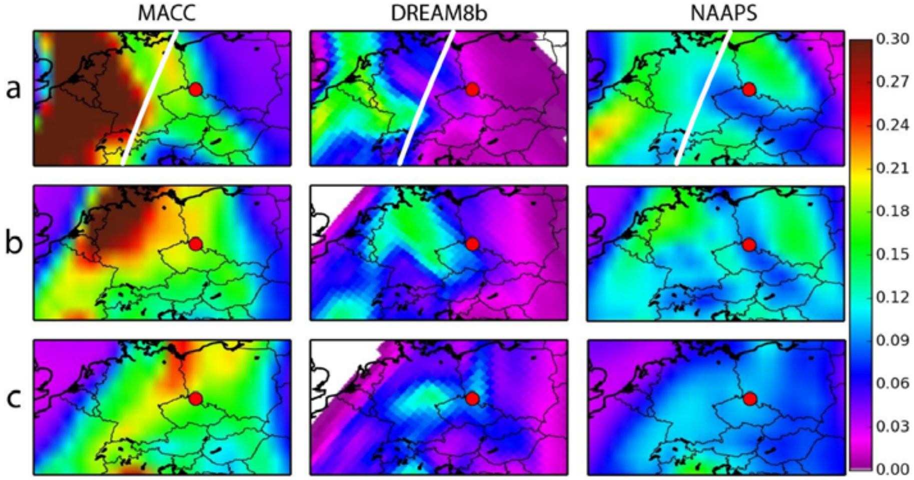

Fig. 8. Mineral dust optical depth at 550 nm between 29 and 30 June 2012 obtained from the MACC, DREAM8b, and NAAPS simulations: (a) 00:00 UTC 29 June 2012, (b) 12:00 UTC 29 June 2012, (c) 00:00 UTC 30 June 2012. For clarity the circle represents the location of the HyMountEcos station in Karpacz. Trajectory of CALYPSO on 29 June 2012 01:30 UTC – white line in panel (a).

(0.15-0.3). The last panel (Fig. 8c) depicts simulations for midnight between 29 and 30 June 2012. All models predicted a decrease of total DOD over Europe and end of dust advection from north-west. MACC simulated highest values of DOD over western borders of Poland, but values in Karpacz are lower than forecasts for previous times. In the DREAM8b and NAAPS simulations, there is a visible decrease of DOD values in most of Europe. However, in the Karpacz area, values are higher than previous time (DREAM8b 0.12, NAAPS 0.11). In the last time step, all three models simulated an area of increased DOD values over North Italy. The source of this increase was the direct transport of dust from Africa to the north, which was independent of the earlier event described above. Complete analysis of predictions by the three models shows that main features of the advection (direction of transport, end of the event), where similar in all models. Deeper comparison reveals discrepancies in spatial and temporal properties of the event. Values of DOD are highest in MACC prediction, reaching 200% of values predicted by NAAPS and DREAM8b. Highest values of DOD predicted by MACC in Central Europe were above 0.30, when NAAPS and DREAM8b proposed ~0.15.

The occurrence of mineral dust over Central Europe was independently confirmed by the CALIOP lidar onboard the CALIPSO satellite. The CALIOP has the ability to collect information on particle linear depolariza-

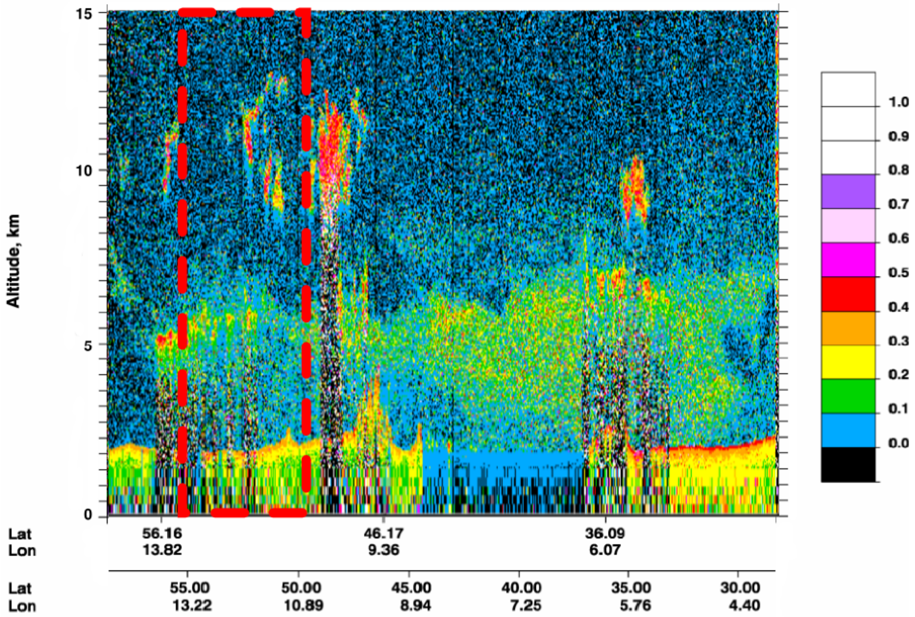

Fig. 9. Transect of particle linear depolarization ratio obtained from CALIOP lidar measurements at 532 nm on 29 June 2012 at 1:30 UTC. Flight path over Central Europe (East Germany). Data from level 2 version 3.02 at 2.5 km horizontal resolution are used here. Central Europe area – red dashed box.

tion ratio at 532 nm, which is helpful in determining the non-sphericity of aerosol particles. On the night of 28/29 June the satellite path crossed Central Europe at 01:30-01:45 UTC. Its overpass was over Central and East Germany, 2.5 degree to the west from Karpacz. The satellite's flight path was not exactly passing over the field station, but according to the HYSPLIT backward trajectories and models simulations, mineral dust was transported over Poland from north-west through Germany. In Fig. 9, illustrating the particle linear depolarization ratio profiles obtained from the CALIOP level 2 data, layers of aerosols with depolarization ratios between 20-30% are visible in the middle troposphere, which is characteristic for Saharan dust (Freudenthaler *et al.* 2009). These layers were observed between 3 and 6 km of altitude, which corresponds with the simulation results (Fig. 6) and seems to be also in accordance with the ground-based observations at the field station near Karpacz (Fig. 12).

5.2 Temporal variability of dust event over Karpacz

Description of temporal changes of the lidar range corrected signal is based on the time composition depicted in Fig. 10a. During the described event, the

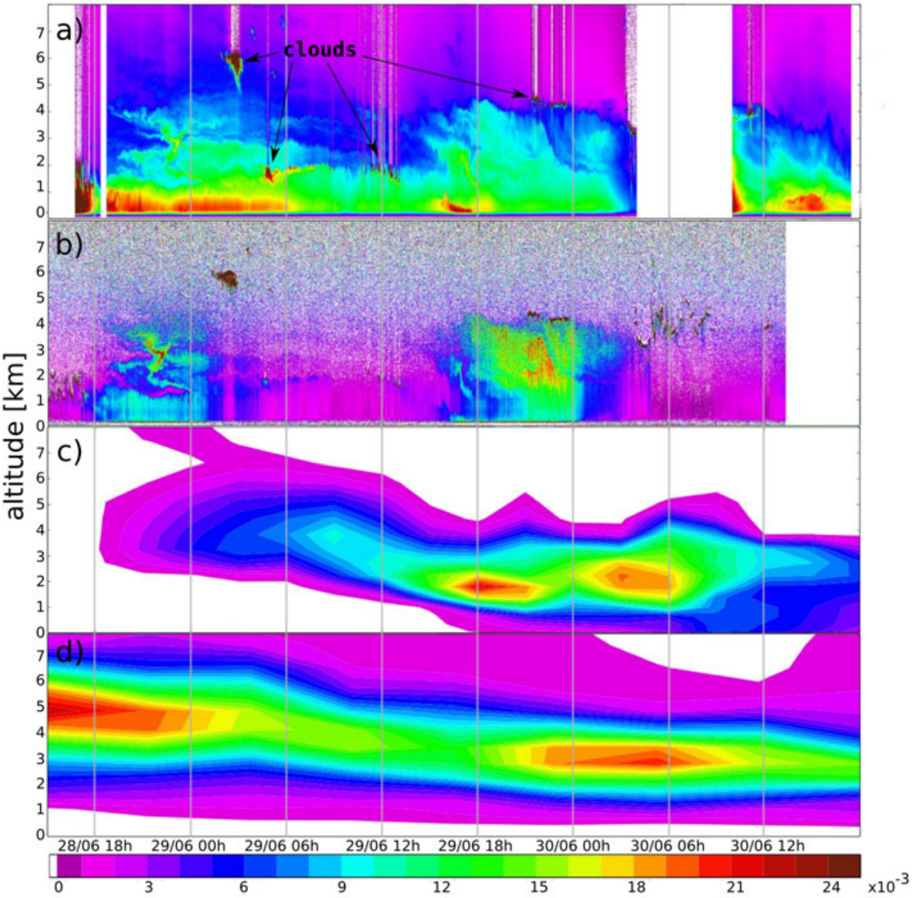

Fig. 10. Temporal variability of vertical structure of the range corrected signal of lidar (a), ceilometer (b), and dust aerosol extinction coefficient [km^{-1}] obtained from the DREAM8b (c) and NAAPS (d) model simulations from 15:00 UTC 28 June 2012 to 18:00 UTC 30 June 2012.

signal above boundary layer (PBL) was mainly dependent on the advected dust concentrations. Lidar measurements with spatial resolution of 7.5 m and time resolution of 1 min provided the most accurate information on this event variability. The first measurements which could be attributed to a dust layer were made before 19:00 UTC on 28 June 2012 at the level of 4 km, and then just before 20:00 UTC an additional layer at 2 km appeared. The intensity of the event has been increasing until midnight. During that time, the observations allowed to distinguish a complicated multilayer structure of dust cloud between 1.5 and 4.5 km. The highest values of the range corrected signal were observed exactly at midnight just below 3 km. After the midnight, the multilayer mixed itself, creating a new layer in the span between 1.5 and 3 km. The high values in the PBL are probably marginally dependent on the dust event (compare with Fig. 10c-d), taking their source most probably from local, likely anthropogenic (coal, oil heating) emissions. This was predicted by NAAPS, which simulated extinction from non-dust particles on the lowest levels. At 06:00 UTC on 29 June 2012, low clouds appeared at 1.5 km level, what made lidar measurements of aerosol particles more difficult to evaluate. The following evening, clouds disappeared at around 18:00 and thus the observations of dust load could be continued. At midnight of 29/30 June 2012 the dust layers were thicker, spanning from 1.2 to 4.5 km, with the main load between 1.5 and 3.5 km. The event was intense during the night of 29/30 June, with a significant decrease of values after 01:30 UTC on 30 June. Note that the gap in lidar measurements between 08:00 and 14:00 on 30 June 2012, is due to a problem with data acquisition. After restart of lidar observations, the dust was still present up to a level of 4 km. Similar vertical structure of aerosol layers has been shown by ceilometer data (Fig. 10b). In this case, a strong range corrected signal appears during nights of 28/29 and 29/30 June. The dust layers between 2 and 4 km are better visible (Fig. 10b) in comparison to lidar data due to larger sensitivity to coarse mode particles and due to neglected Rayleigh scattering. Note that during the daytime the ceilometer has limited sensitivity due to a strong influence of background light on the ceilometer signals.

Figure 10c represents the simulation of the dust event calculated with the use of the DREAM8b model. Extinction coefficient on 24 levels from 0 to 15 km, in intervals of 3 h, was calculated. The model predicted the beginning of the event at 20:00 UTC on 28 June 2012 with an aerosol extinction coefficient of 0.003 km^{-1} at 2.5-5.5 km level. Then, according to simulation, the dust lowered its altitude, reaching the ground at 16:00 on 29 June 2012. The highest peak of aerosol extinction coefficient (more than 0.025 km^{-1}) was simulated from 16:00 to 23:00 UTC on 29 June 2012. The lidar showed high range corrected signal around 19:00 UTC, which generally agreed with the simulation, but was 3 h later than predicted. Afterwards, the simulated event started to weaken. The simulation, in comparison to the lidar measurements, showed an appearance of the dust event later with the clearly visible main load at an altitude of around 2 km, while the lidar detected dust between 0.5 and 4 km, without significant maximum at one altitude.

Figure 10d depicts predictions of extinction coefficient by NAAPS model. The event simulated on this panel started earlier and has local maxima at 18:00 UTC on 28 June with values of extinction coefficient above 0.023 km^{-1} at 5 km altitude. In comparison with observations (Fig. 10a-b) the

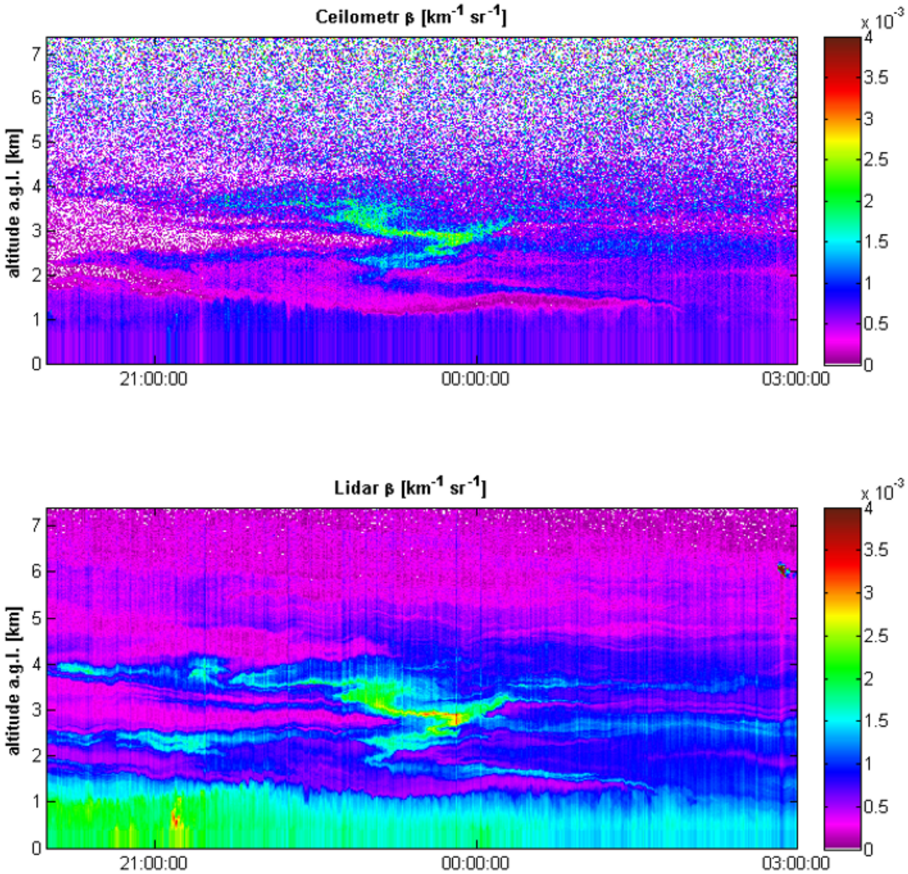

Fig. 11. Aerosol backscatter coefficient retrieved from: (top) ceilometer (1064 nm) and (bottom) lidar (532 nm) observation between 20 UTC 28 June and 2:30 UTC 29 June 2012.

model predicted dust on higher altitude and earlier. Higher values around midnight on 28/29 June better correspond to observations than DREAM8b simulation, which underestimates the intensity of early stages of the dust event. Between 21:00 UTC 29 June and 04:00 UTC 30 June, NAAPS simulated second maxima with values slightly higher than 0.020 km^{-1} between 2 km and 3 km altitude. These maxima correspond with the one simulated by DREAM8b model earlier in a quite similar range. In the whole simulated period, a slow decrease of dust altitude is visible, but it never reached the lowest level.

It is important to remember that the two models operate on a different grid, DREAM8b at 0.33°×0.33° and NAAPS at much sparser grid of 1°×1°;

keeping this in mind, the results from NAAPS show quite accurate prediction of the dust event dynamic with two maxima, but with overestimated altitude of the main dust layer; on the other hand, layers simulated by DREAM8b were on altitudes more similar to measurements, but the maximum at the beginning of the event has not been predicted. Extinction coefficient simulated by DREAM8b and NAAPS reach almost the same values at peaks ~0.022, but NAAPS simulated higher total load with background in the range of 1-7 km of altitude. Temporal variability of results obtained from the lidar measurements clearly shows efficiency of the lidar measurements in determining local diversity of multilayered structure of dust events (Papayannis *et al.* 2007, Guerrero-Rascado *et al.* 2009, Preißler *et al.* 2011).

The temporal evolution of the vertical structure of the retrieved aerosol backscatter coefficients from lidar and ceilometer data is shown in Fig. 11. The upper panel corresponds to the ceilometer backscatter and the bottom one to the lidar backscatter coefficient from 20:00 UTC 28 June 2012 to 02:30 UTC 29 June 2012. We selected this section of measurements for further analysis, because it reveals the most interesting feature of the event. The multilayer of dust particles spans between 2 and 4 km a.g.l. The altitude of almost each aerosol layer decreased with time, which was probably due to air subsidence, advection of the dust to north-west Poland or/and particle sedimentation. Both plots show similar structure of aerosol layers below 4.5 km, especially between 23:00 and 00:30 UTC, when the backscatter coefficient reached the highest values (3.5×10^{-3} – 3.75×10^{-3} km^{-1} sr^{-1} at 532 nm and 2.5×10^{-3} – 2.75×10^{-3} km^{-1} sr^{-1} at 1064 nm).

5.3 Comparison of selected profiles of extinction obtained by model and remote sensors

The comparison of the aerosol extinction coefficient obtained from the lidar and ceilometer measurements and predicted by the DREAM8b and NAAPS models was based on six vertical profiles retrieved during different stages of the dust event. The first three profiles were obtained during the first phase of the dust influx on the night of 28/29 June 2012, and the following three during the event culmination on the night of 29/30 June 2012. The night measurements were selected to avoid problems with high background light affecting ceilometer signals. The aerosol extinction profiles for lidar and ceilometer were calculated with the application of the Klett–Fernald–Sasano algorithm with the AOD calculated as a mean AOD from the NAAPS and MACC simulations for the corresponding corrected wavelengths. Area of uncertainty was defined by standard deviation of the calculated mean AOD. Between simulations time-steps, values were linear interpolated. Profiles were filtered with the Savitzky–Golay algorithm (polynomial of grade 3, data window of 9 measurements). In both cases, a 15 min approximation (±7.5 min) was made, from the hour for which the profile was calculated. Further analyses of obtained profiles are focused on range above PBL (1-1.5 km) due to different overlap function for lidar and ceilometer.

In Fig. 12a, profiles for 28 June 2012 at 22:00 UTC show an extremely low dust load predicted by DREAM8b. On the contrary, the NAAPS model shows a total extinction of 0.052 km^{-1} (0.049 km^{-1} dust) with a maximum at 4.3 km altitude. It is significant that NAAPS predicted increased total extinction coefficient (with a lack of dust) below the PBL which agrees with ob-

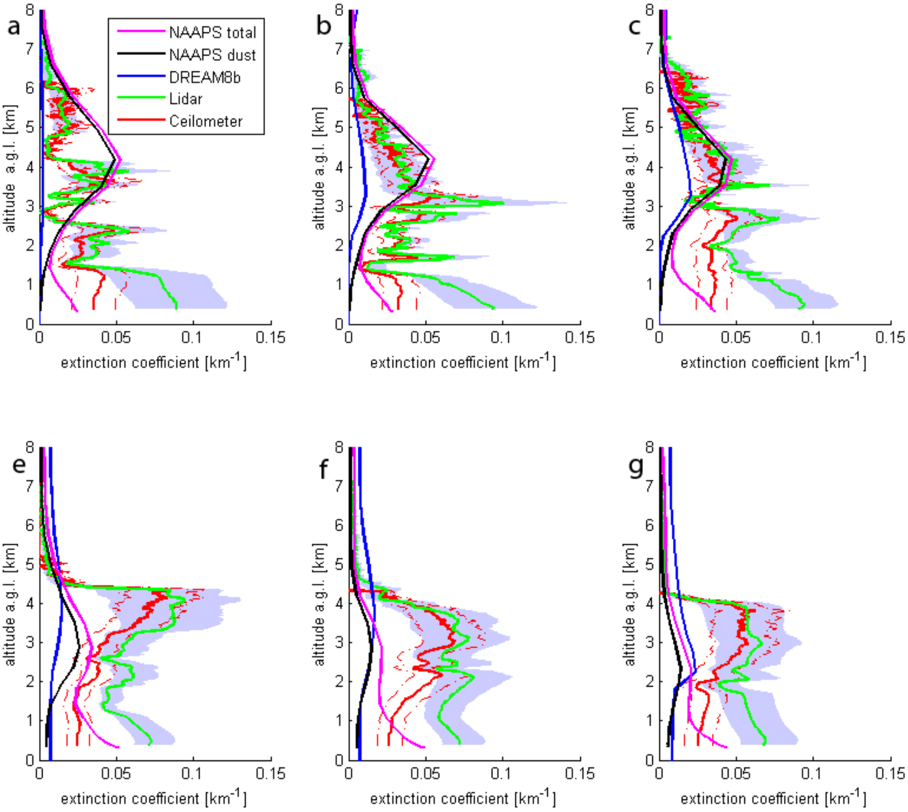

Fig. 12. Aerosol extinction coefficient profiles obtained with the means of lidar at 532 nm (green line), ceilometer at 1064 nm (red line), the DREAM8b model at 550 nm (blue line), the NAAPS model at 550 nm dust extinction coefficient (black line) and NAAPS model total extinction coefficient (magenta line) at 22:00 UTC 28 June (a), 00:30 UTC (b), 02:00 UTC (c), and 21:00 UTC 29 June (d), 00:00 UTC (e), and 04:00 UTC 30 June (f). Gray color and red dotted line represent the area of uncertainty for lidar/ceilometer.

servations based on range corrected signal (Fig. 10). The aerosol extinction profiles, based on both remote sensing measurements, depict some aerosol layers at the range of 1.5-6 km (max 0.058±0.025 km^{-1} at 532 nm and 0.048 ± 0.025 km^{-1} at 1064 nm). The structure presented three layers: 1.5-2.6 km, 3-4.2 km, and 4.8-6 km. Starting from 3.25 km the results from lidar and ceilometer present high similarity of a structure; however, in the upper layers the increase of extinction coefficient obtained from lidar measurement, along with the simultaneous decrease of the extinction coefficient for the ceilometer measurements, may be noticed. This might be caused by the low signal-to-noise ratio of the ceilometer beyond 5 km altitude and by the aerosol advection, which seem to be confirmed by the increase of the aerosol extinction coefficient of lidar at 5-6 km range, however, does not exceed 0.025±0.07 km^{-1}, which is lower by almost a half than at the lower layers at this profile. Differences in profiles below 2 km are caused by different overlap function of both systems and higher number of smaller particles in PBL layer, which are better detected by the shorter wavelength system.

The plot in Fig. 12b depicts results at 00:30 UTC (2.5 h later). Here the first clearly marked increase in the aerosol extinction coefficient value was simulated by the DREAM8b model. The main load of dust was predicted between 2.2 and 5.5 km, with a flat maximum at about 3.4 km and the aerosol extinction coefficient value of about 0.011 km^{-1}. NAAPS predictions were the same in shape as before, with only small decrease of values, 0.055 km^{-1} total extinction and 0.051 km^{-1} dust component. The measurements confirmed the existence of the maximum a little lower, at heights between 3 and 3.3 km, but with substantially higher values of about 0.06 km^{-1} ± 0.023 for ceilometer and 0.1 km^{-1} ± 0.035 for lidar. The course of vertical variability of the extinction coefficient is similar for remote measurements and highlights a few clear local maxima, *e.g.*, at: 1.75, 2.8, and 3.25 km. The high extinction values, confirming the expected transport of the Saharan dust, extend from 1.5 to 5.5 km. The retrieved profile has the highest values of all profiles retrieved during the night of 28/29 June 2012.

In the profile retrieved for the same day at 02:00 UTC (Fig. 12c), 1.5 h later, the maximum values decreased and the vertical structure of aerosol simplified. Values simulated by the DREAM8b model reached the level of 0.021 km^{-1}, remaining at practically the same heights with the maximum at about 3.4 km. NAAPS simulations preserve the earlier shape of the profile, but extinction coefficient decreased to 0.047 km^{-1}. The remote sensors profiles show higher aerosol extinction coefficient than predicted by DREAM8b model, for the entire profile, up to the height of 6.5 km, with two local maxima, at 2.75 and 3.5 km. Results retrieved from remote sensing above 3.5 km fit the values simulated by NAAPS model. The observed remote profiles al-low to discern two thick, homogeneous aerosol layers, divided at a height of 3.1 km by the decrease of aerosol extinction coefficient to a one third (0.025 km^{-1} ± 0.02) of the for the maximum level (0.078 km^{-1} ± 0.023). Nearly similar values of aerosol extinction coefficient for devices operating on different wavelength (lidar – 532 nm, ceilometer – 1064 nm) retrieved during the night of 28/29 June 2012 are characteristic for large particles like the mineral dust.

The following night, on 29/30 June 2012, depicted in Fig. 12d-f, was characterized by substantially higher observed aerosol extinction coefficient values. During this night, the DREAM8b model at 21:00 UTC (Fig. 12d) predicted dust from 2 to 7 km, with a maximum of about 0.015 km^{-1} at about 4.2 km. NAAPS model maximum of 0.035 km^{-1} lowered the altitude and was predicted just below 3 km. The measurements correspond to the DREAM8b simulation, with clearly marked maximum values at about 4.3 km with value of about 0.093 km^{-1} ± 0.03 for lidar and 0.083 km^{-1} ± 0.025 for ceilometer. Both profiles show the upper limit of the dust layer at a height of 4.5 km, above which the signal strength decreased to the noise level. Both profiles are corresponding well to each other, with values almost steadily increasing with the height up to the top of the layer.

The profiles at midnight of 29/30 June 2012 (Fig. 12e) show a larger discrepancy between the modeled and the measured values. In comparison with previous profile (Fig. 12d) the DREAM8b model simulated a steady increase in the aerosol extinction coefficient, with the maximum at the level of 3.8 km and span over 1.8-6.5 km, with maximum value of about 0.019 km^{-1}. Values simulated by NAAPS decreased to 0.021 km^{-1} at the same height as before. For the first time in the analyzed profiles both models show a region of great coherence of simulated dust extinction up to 3 km altitude. The measurements show a decrease of the aerosol extinction coefficient values which have reach the values of about 0.084 km^{-1} ± 0.020 (532 nm) at about 2.1 km and between 2.9-3.7 km and 0.079 km^{-1} ± 0.032 (532 nm) at about 2.5 km. Thus, the aerosol layer is not that uniform as previously and no longer has a clear upper limit. Above 4.7 km it vanishes. As before, the lidar and ceilometer measurements are corresponding above the lowermost 1.5 km well to each other, indicating the main dust load at the range of 2.75-3.75 km, with additional thin layers at 2.25 and 2.5 km. This layers had probably separated from the existing increased aerosol load beyond 2.5 km.

Finally, Fig. 12f shows the data from 04:00 UTC on 30 June 2012. Here the DREAM8b predicted lowering of the dust maximum in terms of its height down to about 2.3 km as well as in terms of the aerosol extinction value as this height range reaches 0.024 km^{-1}. From this point, the values steadily decreased until they reached zero at approximately 6.5 km. NAAPS model simulated lower total extinction with flat maximum of 0.020 km^{-1} at the same altitude as DREAM8b. Shape of both simulated profiles shows great discrepancy. The profile from lidar reveals rather flat maxima at about 3 and 3.8 with the values of 0.065 km^{-1} ± 0.028 and a clear decrease of layer at 4 km. Above, only marginal aerosol load remains up to 6.5 km. The top border of the main dust layer is well-marked. The shape of the ceilometer profile is similar to the one in Fig. 12d, with a steady extinction increase with height. The lidar profile has a more similar structure to profiles in Fig. 12e, with an additionally separated thin layer at about 2.1 km. This layer is probably the same as the one at 2.25 km in Fig. 12e.

The comparison of vertical variability of the extinction coefficient among the lidar, the ceilometer, the DREAM8b model and the NAAPS model measurements allows for the following conclusions: the models present very simplified profiles. Extinction values predicted by DREAM8b model are substantially lower than the observed ones. NAAPS model simulated values closer to the observed ones. In most cases, the DREAM8b model correctly predicted the level of the dust transport, together with the location of its maximum value; however, at times the maximum values were substantially lower, as compared to the observed ones, which has already been observed in other studies (Mona *et al.* 2014). Profiles calculated by NAAPS model show limited coherence with profiles retrieved from remote sensing methods. The profiles based on the remote sensing measurements show great coherence with the vertical variability profiles made with the aid of lidar and ceilometer. Possible errors of retrieved extinction coefficient come from the inevitability of subjectively made assumptions about the initial values, resultant from the lack of remote sensing measurements of the complete optical thickness, which was caused by high clouds covering the sun. Thus, it was impossible to make measurements with a sun-photometer.

5.4 Comparison of the observed and simulated AOD

Based on the retrieved profiles of aerosol extinction coefficient from lidar we estimated the total AOD and the AOD above the PBL. To compute the AOD above the PBL, we integrated each profile of the aerosol extinction coefficient in the range above boundary layer height, which was in general between about 1.5 and 7.5 km. The PBL height was estimated based on the maximum gradient method applied to the range corrected signal (Stachlewska *et al.* 2012). Below the overlap height the aerosol extinction coefficient was assumed constant. Due to very small value of particle linear depolarization ratio from CALIPSO and low concentration of dust simulated by DREAM8b model below 1.5 km, the AOD above the PBL can be interpreted, in the first approximation, as the dust AOD. Figure 13a shows the

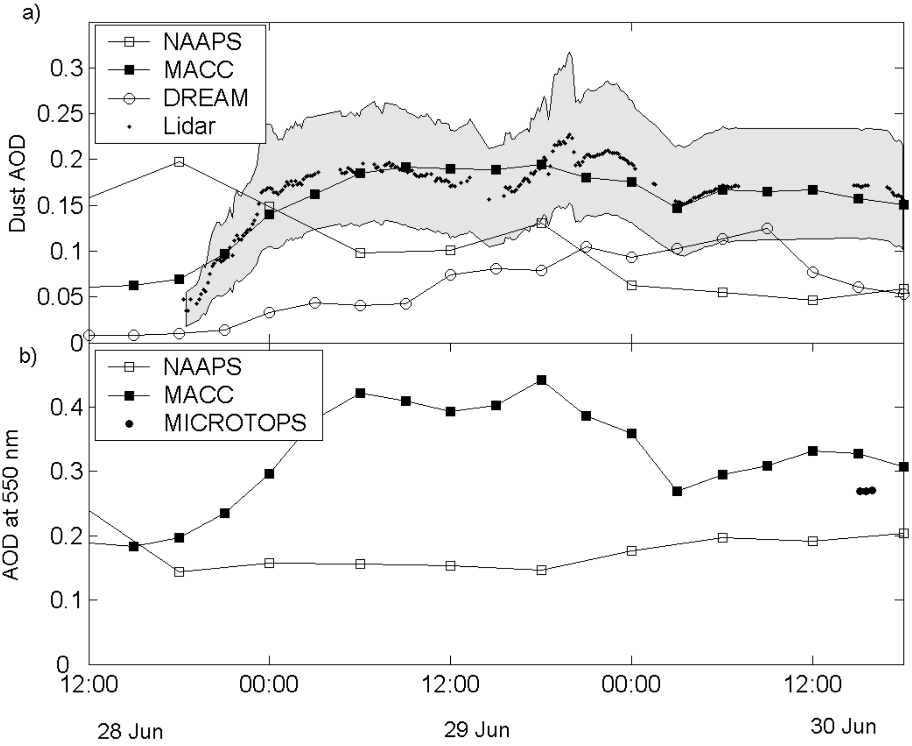

Fig. 13. Temporal variability of: (a) dust AOD and (b) total AOD obtained from the NAAPS (open square line), MACC (solid squared line), DREAM8b model (open circle lines), lidar observation (black dots); and Microtops (dots). Gray color on case of lidar data represents the area of uncertainty.

AOD above the PBL obtained from the NAAPS (line with open squares), MACC (line with solid squares), DREAM8b model (line with circles), and from the lidar (shading). Differences between models and lidar are significant. For example, NAAPS model shows the peak of dust event on 28 June late afternoon while DREAM before noontime of 30 June. The MACC model simulated the beginning of the dust event at midnight 28/29 June and maximum of the dust AOD about 0.2. The lidar AOD above the PBL starts an increase just before the midnight 28/29 similar to MACC model. MACC simulation very well corresponds with lidar measurements reproducing almost the same temporal evolution and values of dust AOD. However, the uncertainty of the dust AOD obtained from lidar measurements is quite large due to high uncertainty of the total AOD applied to Klett–Fernald–Sasano method. Comparison of the total AOD retrieved from NAAPS (line with open squares), MACC (line with solid squares), and the Microtops sun-photometer (dots) (Fig. 13b) reveals similar differences. The AOD from MACC is systematically higher than from NAAPS and a maximum of AOD difference exceeds 0.2 on 29 June. Unfortunately, due to regular occurrence of cirrus clouds, only 3 sun-photometer daytime observations during this dust event were possible. Comparison of the sun-photometer AOD can be done only between 15 and 16 UTC on 30 June. During this period, the NAAPS underestimated the observation AOD by 0.06 and MACC overestimated by 0.04. In case of the Angstrom exponent the NAAPS, MACC, and Microtops values are the following: 0.39, 0.59, and 1.23, respectively. Although the dust AOD contribution to the total AOD is about 50% for MACC and only 25% for NAAPS, the Angstrom exponent estimated from MACC model is significantly higher than from NAAPS. It means that the size distribution of dust particles is dominated by fine mode. In case of DREAM8b we estimated the dust Angstrom exponent of 0.28 which also indicates reduction of large dust particles, in consistence with dust transport. HYSPLIT analysis (Fig. 7) has shown several-day long-range transport trough Western Europe, which enabled a significant part of the coarse-mode dust to be removed.

6. SUMMARY AND FINAL CONCLUSION

In this paper we attempted to provide seasonal variability of dust AOD based on NAAPS and MACC re-analysis. The models are able to reproduce with reasonable skill the observed long term seasonal mean AOD. The comparison with CIMEL sun-photometer measurements shows that the MACC model tends to slighty overestimate the AOD (mean bias is 0.02) and NAAPS to significantly underestimate the AOD (mean bias is 0.1). Similar comparisons for long-term monthly mean value indicate that NAAPS underestimates the CIMEL value by 0.05, especially during spring season (about 30%). For the MACC model we found an overestimation of the AOD in May and June (25-30%) and an underestimation during winter (30-45%). Although the mean AOD bias for MACC is smaller than for the NAAPS model, MACC shows significant inconsistencies with observations during winter. It is probably because of the data assimilation procedures which include the AOD from MODIS observations. The MODIS AOD retrieval is limited only to days with clear sky, which during winter season are usually related to low temperature and high local emissions, which result in smog conditions and high values of AOD; thus in the case of small number of those days, the MODIS assimilation to the MACC can produce some bias. Results from both models are consistent with estimated annual cycles of dust AOD except for the summer months. Simulated dust AOD shows annual cycle with minimum (0.01-0.02) during winter and maximum (about 0.05) during spring and summer. During summer, the dust AODs in case of MACC are about 0.04, while the NAAPS value is about 0.02. Similarly to dust AOD case during summer months, the MACC shows larger dust contribution to the total AOD than NAAPS model. Generally, the MACC dust contribution during spring and summer months is almost flat, while the NAAPS model shows peak value in May.

The annual mean of dust AOD estimated from AERONET and model data is 0.038 ± 0.016. The monthly mean dust AOD has a maximum in April (0.057 ± 0.03) and minimum in December and January 0.027 ± 0.01. The relative number of days with dust event (dust AOD larger than 0.05) is about 28% in May and below 5% in winter. Significant dust events (dust AOD above 0.1) appear during about 9.5% (NAAPS) and 4.5% (MACC) days in May.

The second phase of model validation was based on the HyMountEcos campaign which took place in June 2012. Aerosol optical properties measured by remote sensing instruments and simulated by NAAPS, MACC, and DREAM8b model during the Saharan dust transport were compared. Major correspondences were found in aerosol extinction and backscatter coefficient profiles (shape and values) retrieved from the lidar and ceilometer data. The differences observed in some parts of profiles are characteristic for mineral dust events where larger particles are expected, which results in a relatively high signal at 1064 nm in comparison with 532 nm. Discrepancies in profiles below PBL have their source in different overlap function of both systems and possible appearance of smaller particles from local emissions. The ceilometer detected dust layer above the boundary layer up to 6 km a.g.l. during the night. The comparison of vertical variability of the aerosol extinction coefficient among lidar/ceilometer with the NAAPS and DREAM8b model shows moderate agreement. Differences in values and altitudes of maxima of aerosol backscatter coefficient simulated by the models in comparison to lidar/ceilometer data were found, but the main character of the event was preserved. It is likely due to the model simplifications in dust emissions, deposition and advection parameterization, which are related to the spatial and temporal resolution of the models and often limit their simulation capabilities for processes of larger scale. Although the DREAM8B model includes 8 size bins and NAAPS only one, the profiles of aerosol extinction from NAAPS are more consistent with lidar data. Generally, both the extinction coefficient and dust AOD for DREAM8b data values are smaller than NAAPS data. However, the uncertainty of the dust AOD obtained from Klett–Ferrnald–Sasano method applied to lidar data is large, the results agree quite well with the MACC model. Measurements done with the lidar delivered detailed information on temporal evolution of the dust event with especially interesting data representing multilayered structures of mineral dust transported by the airmass. Thanks to transport of the dust above PBL it was possible to calculate estimated dust AOD from lidar measurements and compare it with values simulated by models.

Acknowledgements. This research was supported with funding of the National Grants No. 1283/B/P01/2010/38 and No. 1276/B/P01/2010/38 of the Ministry of Science and Higher Education of Poland, both coordinated by the IGF UW. We kindly acknowledge the NASA Langley Research Center Atmospheric Science Data Center for the provision of the CALIPSO products used in this study. This work has been supported in part by the European Community under the contract FP7/2007-2013 (MACC project). We acknowledge Brent Holben for the use of the data from the Belsk AERONET station and P. Flatau from Naval Research Laboratory in Monterey for providing NAAPS data.

References

AERONET (2002-2012), AERONET climatology, level 2.0 – quality assured data: Belsk, Aerosol Robotic Network, available from: http://aeronet.gsfc.nasa.gov/new_web/V2/climo_new/Belsk_500.html.

Alpert, P., and B. Ziv (1989), The Sharav cyclone: observations and some theoretical considerations, *J. Geophys. Res.* **94**, D15, 18495-18514, DOI: 10.1029/JD094iD15p18495.

Anderson, J.R., E.E. Hardy, J.T. Roach, and R.E. Witmer (1976), *A Land Use and Land Cover Classification System for Use with Remote Sensor Data*, U.S. Geol. Surv. Prof. Paper, Vol. 964, 28 pp.

Ansmann, A., J. Bösenberg, A. Chaikovsky, A. Comerón, S. Eckhardt, R. Eixmann, V. Freudenthaler, P. Ginoux, L. Komguem, H. Linné, Á.L. Márquez, V. Matthias, I. Mattis, V. Mitev, D. Müller, S. Music, S. Nickovic, J. Pelon, L. Sauvage, P.Sobolewsky, M.K. Srivastava, A. Stohl, O. Torres, G. Vaughan, U. Wandinger, and M. Wiegner (2003), Long-range transport of Saharan dust to northern Europe: The 11-16 October 2001 outbreak observed with EARLINET, *J. Geophys. Res.* **108**, D24, 4783, DOI: 10.1029/2003JD003757.

Balkanski, Y., M. Schulz, T. Claquin, and S. Guibert (2007), Reevaluation of mineral aerosol radiative forcings suggests a better agreement with satellite and AERONET data, *Atmos. Chem. Phys.* **7**, 81-95, DOI: 10.5194/acp-7-81-2007.

Bègue, N., P. Tulet, J.-P. Chaboureau, G. Roberts, L. Gomes, and M. Mallet (2012), Long-range transport of Saharan dust over northwestern Europe during

EUCAARI 2008 campaign: Evolution of dust optical properties by scavenging, *J. Geophys. Res*. **117**, D17, D17201, DOI: 10.1029/2012JD017611.

Bellouin, N., J. Quaas, J.-J. Morcrette, and O. Boucher (2013), Estimates of aerosol radiative forcing from the MACC re-analysis, *Atmos. Chem. Phys*. **13**, 4, 2045-2062, DOI: 10.5194/acp-13-2045-2013.

Benedetti, A., J.-J. Morcrette, O. Boucher, A. Dethof, R.J. Engelen, M. Fisher, H. Flentje, N. Huneeus, L. Jones, J.W. Kaiser, S. Kinne, A. Mangold, M. Razinger, A.J. Simmons, and M. Suttie (2009), Aerosol analysis and forecast in the European Centre for Medium-Range Weather Forecasts Integrated Forecast System: 2. Data assimilation, *J Geophys. Res.* **114**, D13, D13205, DOI: 10.1029/2008JD011115.

Brooks, N., and M. Legrand (2000), Dust variability over northern Africa and rainfall in the Sahel. **In:** S.J. Mc Larsen and D. Kiiverton (eds.), *Linking Land Surface Change to Climate Change*, Kluwer.

Chand, D., R. Wood, T.L. Anderson, S.K. Satheesh, and R.J. Charlson (2009), Satellite-derived direct radiative effect of aerosols dependent on cloud cover, *Nat. Geosci*. **2**, 3, 181-184, DOI: 10.1038/NGEO437.

Chen, L., G. Shi, S. Qin, S. Yang, and P. Zhang (2011), Direct radiative forcing of anthropogenic aerosols over oceans from satellite observations, *Adv. Atmos. Sci*. **28**, 4, 973-984, DOI: 10.1007/s00376-010-9210-4.

Choobari, O.A., P. Zawar-Reza, and A. Sturman (2014), The global distribution of mineral dust and its impacts on the climate system: A review, *Atmos. Res.* **138**, 152-165, DOI: 10.1016/j.atmosres.2013.11.007.

Christensen, J.H. (1997), The Danish Eulerian Hemispheric Model – a three-dimensional air pollution model used for the Arctic, *Atmos. Environ*. **31**, 24, 4169-4191, DOI: 10.1016/S1352-2310(97)00264-1

Di Sarra, A., T. Di Iorio, and M. Cacciani (2001), Saharan dust profiles measured by lidar at Lampedusa, *J. Geophys. Res. Atmos.* **106**, D10, 10335-10347.

Draxler, R.R., and G.D. Rolph (2010), HYSPLIT (HYbrid Single-Particle Lagrangian Integrated Trajectory) Model access via NOAA ARL READY, NOAA Air Resources Laboratory, Silver Spring, MD, available from: http://ready.arl.noaa.gov/HYSPLIT.php.

Duce, R.A. (1995), Sources, distributions, and fluxes of mineral aerosols and their relationship to climate. **In:** R. Charlson and J. Heintzenberg (eds.), *Aerosol Forcing of Climate*, Wiley, New York, 43-72.

Engelstaedter, S., and R. Washington (2007), Atmospheric controls on the annual cycle of North African dust, *J. Geophys. Res. Atmos.* **112**, D3, D03103, DOI: 10.1029/2006JD007195.

Engelstaedter, S., I. Tegen, and R. Washington (2006), North African dust emissions and transport, *Earth Sci. Rev.* **79**, 1-2, 73-100, DOI: 10.1016/j.earscirev.2006.06.004.

Eresmaa, N., A. Karppinen, S.M. Joffre, J. Rasanen, and H. Talvitie (2006), Mixing height determination by ceilometers, *Atmos. Chem. Phys.* **6**, 1485-1493.

Fernald, F.G. (1984), Analysis of atmospheric lidar observations: some comments, *Appl. Opt.* **23**, 5, 652-653.

Flentje, H., B. Heese, J. Reichardt, and W. Thomas (2010), Aerosol profiling using the ceilometer network of the German Meteorological Service, *Atmos. Meas. Tech.* **3**, 3643-3673, DOI: 10.5194/amtd-3-3643-2010.

Formenti, P., J.L. Rajot, K. Desboeufs, S. Caquineau, S. Chevaillier, S. Nava, A. Gaudichet, E. Journet, S. Triquet, S. Alfaro, M. Chiari, J. Haywood, H. Coe, and E. Highwood (2008), Regional variability of the composition of mineral dust from western Africa: Results from the AMMA SOP0/ DABEX and DODO field campaigns, *J. Geophys. Res. Atmos.* **113**, D20, D00C13, DOI: 10.1029/2008JD009903.

Freudenthaler, V., M. Esselborn, M. Wiegner, B. Heese, M. Tesche, A. Ansmann, D. Müller, D. Althausen, M. Wirth, A. Fix, G. Ehret, P. Knippertz, C. Toledano, M. Garhammer, and M. Seefeldner (2009), Depolarization-ratio profiling at several wavelengths in pure Saharan dust during SAMUM 2006, *Tellus B* **61**, 1, 165-179, DOI: 10.1111/j.1600-0889.2008.00396.x.

Frey, S., K. Poenitz, G. Teschke, and H. Wille (2010), Detection of aerosol layers with ceilometer and the recognition of the mixed layer depth. **In:** *Proc. Int. Symp. for Advancement of Boundary Layer Remote (ISARS)*, 3646-3647.

Ginoux, P., M. Chin, I. Tegen, J.M. Prospero, B. Holben, O. Dubovik, and S.-J. Lin (2001), Sources and distributions of dust aerosols simulated with the GOCART model, *J. Geophys. Res.* **106**, D17, 20255-20273, DOI: 10.1029/ 2000JD000053.

Goudie, A.S., and N.J. Middleton (2001), Saharan dust storms: nature and consequences, *Earth Sci. Rev.* **56**, 1-4, 179-204, DOI: 10.1016/S0012-8252 (01)00067-8.

Gross, S., M. Tesche, V. Freudenthaler, C. Toledano, M. Wiegner, A. Ansmann, D. Althausen, and M. Seefeldner (2011), Characterization of Saharan dust, marine aerosols and mixtures of biomass-burning aerosols and dust by means of multi-wavelength depolarization and Raman lidar measurements during SAMUM 2, *Tellus B* **63**, 4, 706-724, DOI: 10.1111/j.1600-0889. 2011.00556.x.

Guerrero-Rascado, L., F.J. Olmo, I. Avilés-Rodríguez, F. Navas-Guzmán, D. Pérez-Ramírez, H. Lyamani, and L. Alados Arboledas (2009), Extreme Saharan dust event over the southern Iberian Peninsula in September 2007: active and passive remote sensing from surface and satellite, *Atmos. Chem. Phys.* **9**, 21, 8453-8469.

Guerrero-Rascado, J.L., M.J. Costa, D. Bortoli, A.M. Silva, H. Lyamani, and L. Alados-Arboledas (2010), Infrared lidar overlap function: an experimental determination, *Opt. Express* **18**, 19, 20350-20359, DOI: 10.1364/ OE.18.020350.

Heese, B., H. Flentje, D. Althausen, A. Ansmann, and S. Frey (2010), Ceilometer-lidar inter-comparision: backscatter coefficient retrieval and signal-to-noise ratio determination, *Atmos. Meas. Tech.* **3**, 3907-3924, DOI: 10.5194/amtd-3-3907-2010.

Heintzenberg, J. (2009), The SAMUM-1 experiment over Southern Morocco: overview and introduction, *Tellus B* **61**, 1, 2-11, DOI: 10.1111/j.1600-0889.2008.00403.x.

Hess, M., P. Koepke, and I. Schult (1998), Optical properties of aerosols and clouds: The software package OPAC, *Bull. Am. Meteorol. Soc.* **79**, 5, 831-844, DOI: 10.1175/1520-0477(1998)079<0831:OPOAAC>2.0.CO;2.

Hogan, T.F., and L.R. Brody (1993), Sensitivity studies of the Navy's global forecast model parameterizations and evaluation of improvements to NOGAPS, *Mon. Weather Rev.* **121**, 8, 2373-2395, DOI: 10.1175/1520-0493(1993)121<2373:SSOTNG>2.0.CO;2.

Hogan, T.F., and T.E. Rosmond (1991), The description of the Navy operational global atmospheric prediction system, *Mon. Weather Rev.* **119**, 8, 1786-1815, DOI: 10.1175/1520-0493(1991)119<1786:TDOTNO>2.0.CO;2.

Holben, B.N., T.F. Eck, I. Slutsker, D. Tanré, J.P. Buis, A. Setzer, E. Vermote, J.A. Reagan, Y.J. Kaufman, T. Nakajima , F. Lavenu, I. Jankowiak, and A. Smirnov (1998), AERONET – A federated instrument network and data archive for aerosol characterization, *Remote Sens. Environ.* **66**, 1, 1-16, DOI: 10.1016/S0034-4257(98)00031-5.

Huang, L., J.H. Jiang, J.L. Tackett, H. Su, and R. Fu (2013), Seasonal and diurnal variations of aerosol extinction profile and type distribution from CALIPSO 5-year observations, *J. Geophys. Res. Atmos.* **118**, 10, 4572-4596, DOI: 10.1002/jgrd.50407.

IPCC (2014), Climate Change 2013: The Physical Science Basis. Contribution of Working Group I to the Fifth Assessment Report of the Intergovernmental Panel on Climate Change (T.F. Stocker, D. Qin, G.-K. Plattner, M. Tignor, S.K. Allen, J. Boschung, A. Nauels, Y. Xia, V. Bex and P.M. Midgley (eds.)), Cambridge University Press, Cambridge, 1535 pp.

Israelevich, P.L., E. Ganor, Z. Levin, J.H. Joseph (2003), Annual variations of physical properties of desert dust over Israel, *J. Geophys. Res.* **108**, D13, 4381, DOI: 10.1029/2002JD003163.

Jimenez, J.L., M.R. Canagaratna, N.M. Donahue, A.S.H. Prevot, Q. Zhang, J.H. Kroll, P.F. DeCarlo, J.D. Allan, H. Coe, N.L. Ng, A.C. Aiken, K.S. Docherty, I.M. Ulbrich, A.P. Grieshop, A.L. Robinson, J. Duplissy, J.D. Smith, K.R. Wilson, V.A. Lanz, C. Hueglin, Y.L. Sun, J. Tian, A. Laaksonen, T. Raatikainen, J. Rautiainen, P. Vaattovaara, M. Ehn, M. Kulmala, J.M. Tomlinson, D.R. Collins, M.J. Cubison, E.J. Dunlea, J.A. Huffman, T.B. Onasch, M.R. Alfarra, P.I. Williams, K. Bower, Y. Kondo, J. Schneider, F. Drewnick, S. Borrmann, S. Weimer, K. Demerjian, D. Salcedo, L. Cottrell, R. Griffin, A. Takami, T. Miyoshi,

S. Hatakeyama, A. Shimono, J.Y. Sun, Y.M. Zhang, K. Dzepina, J.R. Kimmel, D. Sueper, J.T. Jayne, S.C. Herndon, A.M. Trimborn, L.R. Williams, E.C. Wood, A.M. Middlebrook, C.E. Kolb, U. Baltensperger, and D.R. Worsnop (2009), Evolution of organic aerosols in the atmosphere, *Science* **326**, 5959, 1525-1529, DOI: 10.1126/science.1180353.

Kandler, K., L. Schuetz, C. Deutscher, M. Ebert, H. Hofmann, S. Jackel, R.P. Knippertz, K. Lieke, A. Masling, A. Petzold, A. Schladitz, B. Weinzier, A. Wiedensohler, S. Zorn, and S. Weinbruch (2009), Size distribution, mass concentration, chemical and mineralogical composition and derived optical parameters of the boundary layer aerosol at Tinfou, Morocco, during SAMUM 2006, *Tellus B* **61**, 1, 32-50, DOI: 10.1111/j.1600-0889.2008.00385.x.

Klett, J.D. (1985), Lidar inversions with variable backscatter/extinction values, *Appl. Opt.* **24**, 11, 211-220, DOI: 10.1364/AO.24.001638.

Landulfo, E., A. Papayannis, P. Artaxo, A.D.A. Castanho, A.Z. de Freitas, R.F. Souza, N.D. Vieira Junior, M.P.M.P. Jorge, O.R. Sánchez-Ccoyllo, and D.S. Moreira (2003), Synergetic measurements of aerosols over São Paulo, Brazil using LIDAR, sunphotometer and satellite data during the dry season, *Atmos. Chem. Phys.* **3**, 5, 1523-1539, DOI: 10.5194/acp-3-1523-2003.

Lopes, F.J.S., E. Landulfo, and M.A. Vaughan (2013), Evaluating CALIPSO's 532 nm lidar ratio selection algorithm using AERONET sun photometers in Brazil, *Atmos. Meas. Tech.* **6**, 11, 3281-3299, DOI: 10.5194/amt-6-3281-2013.

Maciszewska, A., K. Markowicz, and M. Witek (2010), Multi year analysis of the aerosol optical thickness over Europe, *Acta Geophys.* **58**, 6, 1147-1163, DOI: 10.2478/s11600-010-0034-5.

Marécal, V., V.H. Peuch, C. Andersson, S. Andersson, J. Arteta *et al.* (2015), A regional air quality forecasting system over Europe: the MACC-II daily ensemble production. *Geosci. Model Dev.* **8**, 9, 2777-2813, DOI: 10.5194/gmd-8-2777-2015.

Markowicz, K.M., P.J. Flatau, A.M. Vogelmann, P.K. Quinn, and D. Bates (2003), Modeling and observations of infrared radiative forcing during ACE-Asia, *Quart. J. Roy. Meteorol. Soc.* **129**, 594, 2927-2947.

Markowicz, K.M., P.J. Flatau, A.E. Kardas, K. Stelmaszczyk, and L. Woeste (2008), Ceilometer retrieval of the boundary layer vertical aerosol extinction structure, *J. Atmos. Ocean. Techn.* **25**, 6, 928-944, DOI: 10.1175/ 2007JTECHA 1016.1.

Markowicz, K.M., T. Zielinski, S. Blindheim, M. Gausa, A.K. Jagodnicka, A.E. Kardas, W. Kumala, Sz.P. Malinowski, M. Posyniak, T. Petelski, and T. Stacewicz (2012), Study of vertical structure of aerosol optical properties by sun photometers and ceilometer during macron campaign in 2007, *Acta Geophys.* **60**, 5, 1308-1337, DOI: 10.2478/s11600-011-0056-7.

Marsham, J.H., D.J. Parker, C.M. Grams, C.M. Taylor, and J.M. Haywood (2008), Uplift of Saharan dust south of the intertropical discontinuity, *J. Geophys. Res. Atmos.* **113**, D21, D21102.

Marsham, J.H., M. Hobby, C.J.T. Allen, J.R., Banks, M. Bart *et al.* (2013), Meteorology and dust in the central Sahara: Observations from Fennec supersite-1 during the June 2011 Intensive Observation Period, *J. Geophys. Res.* **118**, 10, 4069-4089, DOI: 10.1002/jgrd.50211.

Martucci, G., C. Milroy, and C.D. O'Dowd (2010), Detection of cloud-base height using Jenoptik CHM15K and Vaisala CL31 ceilometers, *J. Atmos. Ocean. Technol.* **2**, 305-318.

McConnell, C.L., E.J. Highwood, H. Coe, P. Formenti, B. Anderson *et al.* (2008), Seasonal variations of the physical and optical characteristics of Saharan dust: Results from the Dust Outflow and Deposition to the Ocean (DODO) experiment, *J. Geophys. Res.* **113**, D14, DOI: 10.1029/2007JD009606.

McKendry, I.G., D. van der Kamp, K.B. Strawbridge, A. Christen, and B. Crawford (2009), Simultaneous observations of boundary-layer aerosol layers with CL31 ceilometer and 1064/532 nm lidar, *Atmos. Environ.* **43**, 36, 5847-5852, DOI: 10.1016/j.atmosenv.2009.07.063.

Mona, L., Z. Liu, D. Müller, A. Omar, A. Papayannis, G. Pappalardo, N. Sugimoto, and M. Vaughan (2012), Lidar measurements for desert dust characterization: an overview, *Adv. Meteorol.* **2012**, 356265, DOI: 10.1155/2012/356265.

Mona, L., N. Papagiannopoulos, S. Basart, J. Baldasano, and I. Binietoglou *et al.* (2014), EARLINET dust observations vs. BSC-DREAM8b modeled profiles: 12-year-long systematic comparison at Potenza, Italy, *Atmos. Chem. Phys.* **14**, 16, 8781-8793, DOI: 10.5194/acp-14-8781-2014.

Morcrette, J.-J. *et al.* (2009), Aerosol analysis and forecast in the European centre for medium-range weather forecasts integrated forecast system: forward modeling, *J. Geophys. Res.* **114**, D06206, DOI: 10.1029/2008JD011235.

Morys, M., Mims III, F.M. Hagerup, S. Anderson, S.E. Baker, A. Kia, and J. Walkup (2001), Design calibration, and performance of MICROTOPS II handheld ozone monitor and Sun photometer, *J. Geophys. Res.* **106**, D13, 14573-14582, DOI: 10.1029/2001JD900103.

Münkel, C., S. Emeis, W.J. Mueller, and K.P. Schaefer (2004), Aerosol concentration measurements with a lidar ceilometer: Results of a one year measuring campaign. **In:** K. Schaefer *et al.* (eds.), Remote Sensing of Clouds and the Atmosphere VIII, International Society for Optical Engineering (*SPIE Proc.* **5235**), 486-496.

Nickovic, S., G. Kallos, A. Papadopoulos, and O. Kakaliagou (2001), A model for prediction of desert dust cycle in the atmosphere, *J. Geophys. Res. Atmos.* **106**, D16, 18113-118129, DOI: 10.1029/2000JD900794.

O'Connor, E.J., A.J. Illingworth, and R.J. Hogan (2004), A technique for autocalibration of cloud lidar, *J. Atmos. Ocean. Technol.* **21**, 5, 777-786, DOI: 10.1175/1520-0426(2004)021<0777:ATFAOC>2.0.CO;2.

Osborne, S.R., B.T. Johnson, J.M. Haywood, A.J. Baran, M.A.J. Harrison *et al.* (2008), Physical and optical properties of mineral dust aerosol during the Dust and Biomass-burning Experiment, *J. Geophys. Res.* **113**, D00C03, DOI: 10.1029/2007JD009551.

Papayannis, A., D. Balis, V. Amiridis, G. Chourdakis, G. Tsaknakis, C. Zerefos, A.D.A. Castanho, S. Nickovic, S. Kazadzis, and J. Grabowski (2005), Measurements of Saharan dust aerosols over the Eastern Mediterranean using elastic backscatter-Raman lidar, spectrophotometric and satellite observations in the frame of the EARLINET project, *Atmos. Chem. Phys.* **5**, 8, 2065-2079.

Papayannis, A., H.Q. Zhang, V. Amiridis, H.B. Ju, G. Chourdakis, G. Georgoussis, C. Pérez, H.B. Chen, P. Goloub, R.E. Mamouri, S. Kazadzis, D. Paronis, G. Tsaknakis, and J.M. Baldasano (2007), Extraordinary dust event over Beijing, China, during April 2006: Lidar, Sun photometric, satellite observations and model validation, *J. Geophys. Res.* **34**, 7, L07806, DOI: 10.1029/2006GL029125.

Papayannis, A., V. Amiridis, L. Mona, G. Tsaknakis, D. Balis, J. Bösenberg, A. Chaikovski, F. De Tomasi, I. Grigorov, I. Mattis, V. Mitev, D. Müller, S. Nickovic, C. Pérez, A. Pietruczuk, G. Pisani, F. Ravetta, V. Rizi, M. Sicard, T. Trickl, M.Wiegner, and M. Gerding (2008), Systematic lidar observations of aerosol optical properties during Saharan dust intrusions over Europe, in the frame of EARLINET (2000-2002): Statistical analysis and results, *J. Geophys. Res.* **113**, D10, D10204, DOI: 10.1029/2007JD009028.

Pappalardo, G., L. Mona, G. D'Amico, U. Wandinger, M. Adam,A. Amodeo *et al.* (2013), Four-dimensional distribution of the 2010 Eyjafjallajökull volcanic cloud over Europe observed by EARLINET, *Atmos. Chem. Phys.* **13**, 8, 4429-4450, DOI: 10.5194/acp-13-4429-2013.

Pavese, G., M. Calvello, F. Esposito, L. Leone, and R. Restieri (2012), Effects of Saharan dust advection on atmospheric aerosol properties in the West-Mediterranean area, *Adv. Meteorol.* **2012**, 730579, DOI: 10.1155/2012/730579.

Perez, C., S. Nickovic, G. Pejanovic, J. M. Baldasano, and E. Ozsoy (2006a), Interactive dust-radiation modeling: A step to improve weather forecasts, *J. Geophys. Res*. **111**, D16, D16206, DOI: 10.1029/2005JD006717.

Perez, C., S. Nickovic, J.M. Baldasano, M. Sicard, F. Rocadenbosch, and V.E. Cachorro (2006b), A long Saharan dust event over the western Mediterranean: Lidar, Sun photometer observations, and regional dust modeling, *J. Geophys. Res.* **111**, D15, D15214, DOI: 10.1029/2005JD006579.

Pisani, G., A. Boselli, N. Spinelli, and X. Wang (2011), Characterization of Saharan dust layers over Naples (Italy) during 2000-2003 EARLINET project, *Atmos. Res.* **102**, 3, 286-299, DOI: 10.1016/j.atmosres.2011.07.012.

Preißler, J., F. Wagner, S.N. Pereira, and J.L. Guerrero-Rascado (2011), Multi-instrumental observation of an exceptionally strong Saharan dust outbreak over Portugal, *J. Geophys. Res.* **116**, D24, D24204, DOI: 10.1029/2011JD016527.

Prospero, J.M., P. Ginoux, O. Torres, S.E. Nicholson, and T.E. Gill (2002), Environmental characterization of global sources of atmospheric soil dust identified with the Nimbus 7 total ozone mapping spectrometer (toms) absorbing aerosol product, *Rev. Geophys.* **40**, 1, 2-1-2-31, DOI: 10.1029/2000RG000095.

Sasano, Y., E.V. Browell, and S. Ismail (1985), Error caused by Rusing a constant extinction/backscattering ratio in the lidar solution, *Appl. Opt.* **24**, 22, 3929-3932, DOI: 10.1364/AO.24.003929.

Schutgens, N., M. Nakata, and T. Nakajima (2012), Estimating aerosol emissions by assimilating remote sensing observations into a global transport model, *Remote Sens.* **4**, 11, 3528-3543, DOI: 10.3390/rs4113528.

Shifrin, K.S. (1995), Simple relationships for the Angstrom parameter of disperse systems, *Appl. Opt.* **34**, 21, 4480-4485, DOI: 10.1364/AO.34.004480.

Sinha, P., D. Kaskaoutis, R. Manchanda, and S. Sreenivasan (2012), Characteristics of aerosols over Hyderabad in southern Peninsular India: synergy in the classification techniques, *Ann. Geophys.* **30**, 9, 1393-1410, DOI: 10.5194/angeo-30-1393-2012.

Smirnov, A., B.N. Holben, T.F. Eck, O. Dubovik, and I. Slutsker (2000), Cloud screening and quality control algorithms for the AERONET database, *Rem. Sens. Env.* **73**, 3, 337-349, DOI: 10.1016/S0034-4257(00)00109-7.

Stachlewska, I.S., and C. Ritter (2010), On retrieval of lidar extinction profiles using Two-Stream and Raman techniques, *Atmos. Chem. Phys.* **10**, 6, 2813-2824, DOI: 10.5194/acp-10-2813-2010.

Stachlewska, I.S., K.M. Markowicz, and M. Piądłowski (2010), On forward Klett's inversion of ceilometer signals. **In:** *25th ILRC International Laser Radar Conference, 5-9 July 2010, St. Petersburg, Russia.*

Stachlewska, I.S., M. Piądłowski, S. Migacz, A. Szkop, A.J. Zielińska, and P.L. Swaczyna (2012), Ceilometer observations of the boundary layer over Warsaw, Poland, *Acta Geophys.* **60**, 5, 1386-1412, DOI: 10.2478/s11600-012-0054-4.

Sundström, A.-M., T. Nousiainen, and T. Petäjä (2009), On the quantitative lowlevel aerosol measurements using ceilometer-type lidar, *J. Atmos. Ocean. Technol.* **26**, 11, 2340-2352, DOI: 10.1175/2009JTECHA1252.1.

Tegen, I., K. Schepanski, and B Heinold (2013), Comparing two years of Saharan dust source activation obtained by regional modelling and satellite observations, *Atmos. Chem. Phys.* **13**, 5, 2381-2390, DOI: 10.5194/acp-13-2381-2013.

Tesche, M., A. Ansmann, D. Mueller, D. Althausen, I. Mattis *et al*. (2009), Vertical profiling of Saharan dust with Raman lidars and airborne HSRL in southern Morocco during SAMUM, *Tellus B* **61**, 1, 144-164, DOI: 10.1111/j.1600-0889.2008.00390.x.

Varga, G., J. Kovács, and G. Újvári (2013), Analysis of Saharan dust intrusions into the Carpathian Basin (Central Europe) over the period of 1979-2011, *Global Planet Change* **100**, 333-342, DOI: 10.1016/j.gloplacha.2012. 11.007.

Vogelmann, A., P. Flatau, M. Szczodrak, K. Markowicz, and P. Minnett (2003), Observations of large greenhouse effects for anthropogenic aerosols, *Geophys. Res. Lett.* **30**, 12, 1654-1657.

Wagner, F., and A.M. Silva (2008), Some considerations about Angström exponent distributions, *Atmos. Chem. Phys*. **8**, 3, 481-489.

Wandinger, U., and A. Ansmann (2002), Experimental determination of the lidar overlap profile with Raman lidar, *Appl. Opt*. **41**, 3, 511-514, DOI: 10.1364/AO.41.000511.

Wang, X., A. Boselli, L. D'Avino, G. Pisani, N. Spinelli, A. Amodeo, A. Chaikovsky, M. Wiegner, S. Nickovic, A. Papayannis, M.R. Perrone, V. Rizi, L. Sauvage, and A. Stohl (2008), Volcanic dust characterization by EARLINET during Etna's eruptions in 2001-2002, *Atmos. Environ*. **42**, 5, 893-905, DOI: 10.1016/j.atmosenv.2007.10.020.

Wang, Z., H.H. Zhang, X. Jing, and X. Wei (2013), Effect of non-spherical dust aerosol on its direct radiative forcing, *Atmos. Res.* **120**, 112-126, DOI: 10.1016/j.atmosres.2012.08.006.

Weitkamp, C. (ed.) (2005), Lidar: Range-resolved Optical Remote Sensing of the Atmosphere, Springer, New York.

Westphal, D.L., O.B. Toon, and T.N. Carlson (1988), A case study of mobilization and transport of Saharan dust, *J. Atmos. Sci.* **45**, 15, 2145-2175, DOI: 10.1175/1520-0469(1988)045<2145:ACSOMA>2.0.CO;2.

Wiegner, M., and A. Geiß (2012), Aerosol profiling with the Jenoptik ceilometer CHM15kx, *Atmos. Meas. Tech.* **5**, 8, 1953-1964, DOI: 10.5194/amt-5-1953-2012.

Witek, M.L., P.J. Flatau, P.K. Quinn, and D.L. Westphal (2007), Global sea-salt modeling: Results and validation against multicampaign shipboard measurements, *J. Geophys. Res*. **112**, D8, D08215, DOI: 10.1029/2006JD 007779.

Wong, M.S., M.I. Shahzad, J.E. Nichol, K.H. Lee, and P.W. Chan (2013), Validation of MODIS, MISR, OMI, and CALIPSO aerosol optical thickness using ground-based sunphotometers in Hong Kong, *Int. J. Remote Sens*. **34**, 3, 897-918, DOI: 10.1080/01431161.2012.720739.

Zawadzka, O., K. Markowicz, A. Pietruczuk, T. Zielinski, and J. Jaroslawski (2013), Impact of urban pollution emitted in Warsaw on aerosol properties, *Atmos. Environ*. **69**, 15-28, DOI: 10.1016/j.atmosenv.2012.11.065.

Zhang, J., J.S. Reid, D.L. Westphal, N.L. Baker, and E.J. Hyer (2008), A system for operational aerosol optical depth data assimilation over global oceans, *J. Geophys. Res*. **113**, D10, D10208, DOI: 10.1029/2007JD009065.

Received 7 February 2015
Received in revised form 12 November 2015
Accepted 8 December 2015